



# Aging of droplet size distribution in stratocumulus clouds: regimes of droplet size distribution evolution

Jung-Sub Lim<sup>1,a,b</sup> and Fabian Hoffmann<sup>2</sup>

<sup>1</sup>Meteorologisches Institut, Ludwig-Maximilians-Universität München, Munich, Germany

<sup>2</sup>Freie Universität Berlin, Berlin, Germany

<sup>a</sup>now at: NOAA Chemical Science Laboratory, Boulder, CO, USA

<sup>b</sup>now at: Cooperative Institute for Research in Environmental Sciences, University of Colorado, Boulder, CO, USA

**Correspondence:** Jung-Sub Lim (jung-sub.lim@noaa.gov) and Fabian Hoffmann (f.hoffmann@fu-berlin.de)

Received: 7 December 2025 – Discussion started: 23 December 2025

Revised: 6 March 2026 – Accepted: 5 April 2026 – Published: 22 April 2026

**Abstract.** The climatic impact of maritime stratocumulus clouds depends on the evolution of their droplet size distribution (DSD), yet the mechanisms controlling their variability during evaporation remain poorly constrained. Using large-eddy simulations coupled with a Lagrangian cloud model, we demonstrate that the DSD evolution follows two primary regimes: adiabatic growth and entrainment–descent. Within the latter, DSD evolution follows divergent pathways determined by the parcel’s entrainment history: strong entrainment-driven dilution near the cloud top causes rapid broadening, whereas large-scale boundary-layer descent leads to gradual evaporation. Our Lagrangian analysis of the Damköhler number reveals that the commonly observed vertical transition from inhomogeneous to homogeneous mixing signatures does not necessarily reflect a change in the local mixing mechanism. Instead, it results from the vertical sorting of parcels with divergent histories. Parcels subject to strong entrainment retain inhomogeneous signatures throughout their descent, while those experiencing minimal dilution exhibit homogeneous-like characteristics regardless of altitude. This distinction helps resolve ambiguities in interpreting in situ observations where mixing history is often unknown. Finally, we propose a combined analytical–empirical formulation that captures the relative dispersion during both growth and evaporation.

## 1 Introduction

Maritime stratocumulus (Sc) clouds play a key role in Earth’s climate by cooling the planet through the reflection of large amounts of incoming solar radiation (Chen et al., 2000; Siebesma et al., 2004; Wood, 2012). Stratocumulus-topped boundary layers (STBLs) are characterized by a Rayleigh–Bénard-type circulation, driven predominantly by longwave radiative cooling at the cloud top (e.g. Wood, 2012; Mellado, 2017). This circulation is characterized by broad, cloud-laden updrafts and narrow, nearly cloud-free downdrafts known as *cloud holes* (e.g. Krueger, 1993; Korolev and Mazin, 1993; Gerber et al., 2005). As droplets cycle through this dynamic environment, they undergo activation,

condensational growth, entrainment-driven evaporation, and circulation-induced descent, leading to systematic changes in the droplet size distribution (DSD). The DSD fundamentally governs cloud optical properties (Considine and Curry, 1996; Pawlowska et al., 2006; Chandrakar et al., 2022) and precipitation initiation (Seifert and Beheng, 2006).

To capture the time-dependent transformation of cloud microphysics, we define “DSD aging” as the temporal evolution of its shape. Although this concept has previously been introduced in the context of precipitation initiation (Seifert and Beheng, 2006), we specifically use it here to describe the microphysical evolution of the DSD driven by condensation, evaporation, entrainment, and mixing. We characterize DSD aging using two key parameters: the arithmetic mean

droplet radius ( $r_m = \langle r \rangle$ ) and the relative dispersion ( $d_r$ ), defined as the ratio of the standard deviation to the mean radius. The relative dispersion  $d_r$  describes the relative width of the size distribution. It is a key determinant of both cloud optical properties and rain initiation (Liu and Daum, 2004; Liu et al., 2008; Wang et al., 2021), yet it is rarely predicted in conventional moment-based microphysical models. Therefore, understanding DSD aging within the STBL is essential for improving cloud–aerosol–precipitation interactions in climate models, as it links intricate DSD shapes to more predictable boundary layer dynamics.

Previous studies indicate that the correlation between  $d_r$  and mean droplet size varies with dominant microphysical processes and environmental conditions, often shifting between positive and negative across different stages of droplet evolution (Chandrarak et al., 2018; Lu et al., 2020; Luo et al., 2022). We note that some prior studies utilize the volume-mean radius ( $r_v = \langle r^3 \rangle^{1/3}$ ), which is weighted toward larger droplets (e.g. Chandrarak et al., 2018; Lu et al., 2020). While  $r_v \geq r_m$ , both metrics generally capture similar evolutionary trends in this context. Focusing on  $r_m$ , specifically within an adiabatically ascending parcel, condensational growth leads to an increase in  $r_m$  while  $d_r$  decreases. This occurs because smaller droplets grow faster, causing the DSD to narrow (Yau and Rogers, 1996). This inverse relationship is well-characterized by existing analytical expressions (Liu et al., 2006).

However, during entrainment and mixing, the changes in  $r_m$  and  $d_r$  become more complex and less predictable. This complexity arises because entrainment is a non-adiabatic and intermittent process. The amount of free-tropospheric air that is entrained, the rate at which it mixes with cloudy air, and the timescale over which the mixture approaches thermodynamic equilibrium, all of which are critical for understanding how entrainment and mixing influence DSD shape, remain poorly constrained in both observations and models. In addition, the specific mixing scenario further complicates predictions. Under homogeneous mixing,  $r_m$  typically decreases and  $d_r$  increases as all droplets partially evaporate (Baker and Latham, 1979). In contrast, inhomogeneous mixing may leave both parameters largely unchanged while decreasing the droplet number concentration through the complete evaporation of some droplets (Baker and Latham, 1979; Baker et al., 1980; Lehmann et al., 2009). Even  $r_m$  can increase and  $d_r$  decrease in a “narrowing” mixing scenario as suggested in a recent study (Lim and Hoffmann, 2023). In situ measurements often reveal inhomogeneous mixing signatures near the cloud top and homogeneous characteristics below (Wang et al., 2009; Yum et al., 2015; Yeom et al., 2021). However, it remains unclear whether this reflects a true change in the physical mixing mechanism or results from other processes, such as dilution or the vertical sorting of parcels with different mixing histories. Therefore, to understand the spatiotemporal variability of  $d_r$  in stratocumulus clouds, it is essential

to resolve how entrainment and mixing interact with the Lagrangian history of the droplets.

In this study, we employ the  $L^3$  model (Hoffmann et al., 2019; Hoffmann and Feingold, 2019; Lim and Hoffmann, 2023, 2024), a novel framework that combines large-eddy simulation (LES) with a linear eddy model (LEM) and a Lagrangian cloud model (LCM). The  $L^3$  model explicitly resolves subgrid-scale (SGS) supersaturation ( $S$ ) fluctuations and turbulent mixing using the LEM, which mimics fine-scale turbulent stirring and scalar transport (Kerstein, 1988). The LCM tracks individual hydrometeors (e.g. Hoffmann et al., 2015), represented as computational particles that stand in for ensembles of real droplets or aerosols (Shima et al., 2009), thereby capturing detailed microphysical processes. This Lagrangian approach enables us to track individual particles along their trajectories through the STBL vertical circulation, capturing the evolving thermodynamic and microphysical conditions that govern droplet growth. In particular, it allows for a detailed quantification of how the DSD shape evolves along distinct pathways shaped by droplet activation, condensation, entrainment, mixing, and evaporation.

This paper is structured as follows. Section 2 presents the  $L^3$  model framework and simulation settings. Section 3 shows how the DSD shape parameters evolve in different regimes. In Sect. 4, we discuss a method to predict  $d_r$  in these regimes. Finally, we conclude our paper in Sect. 5. Parts of this study are based on the first author’s dissertation (Lim, 2024), which has been extended with special attention to the impact of different mixing pathways (Sect. 3.3.3 and 3.4) and more general conclusions (Sect. 5).

## 2 Model and Simulations

### 2.1 The $L^3$ model

We employ the novel  $L^3$  model (Hoffmann et al., 2019), built upon the System for Atmospheric Modeling (SAM), a nonhydrostatic, anelastic LES model (Khairoutdinov and Randall, 2003). Cloud microphysical processes are modeled using the LCM, employing individually simulated computational particles, i.e. LCM particles, where each particle represents a group of identical hydrometeors. Additionally, the linear eddy model (LEM), an explicit turbulence and mixing model (Kerstein, 1988; Krueger et al., 1997), is coupled with the LCM and LES to represent the unresolved effects of entrainment and mixing on droplet growth (Hoffmann et al., 2019; Hoffmann and Feingold, 2019; Lim and Hoffmann, 2023, 2024).

In the Lagrangian Cloud Model (LCM), condensational growth of droplets is driven by the supersaturation,

$$S = \bar{S} + S', \quad (1)$$

where the LES-resolved mean supersaturation is

$$\bar{S} = \frac{\bar{q}_v}{q_s(\bar{T}, p)} - 1. \quad (2)$$

Here,  $\bar{q}_v$  is the LES-resolved water vapor mixing ratio, and  $q_s$  is the saturation vapor mixing ratio determined by the LES-resolved temperature  $\bar{T}$  and pressure  $p$ . The fluctuation term  $S'$  represents the deviation from  $\bar{S}$  and is tracked individually for each LCM particle, being updated continuously throughout its growth history. The LEM redistributes  $S'$  among the LCM particles by mimicking turbulent compression and folding based on the LES subgrid turbulence kinetic energy. Therefore, in the  $L^3$  model, droplet condensational growth is determined by both  $\bar{S}$  and  $S'$ , allowing for a realistic representation of different mixing scenarios during entrainment and mixing (Lim and Hoffmann, 2023, 2024). Moreover, the standard deviation of supersaturation,  $\sigma_S$ , defined as the standard deviation of  $S = \bar{S} + S'$ , is inherently resolved by the  $L^3$  model. Further details on the  $L^3$  framework can be found in Hoffmann et al. (2019).

## 2.2 Simulation Setup

A maritime nocturnal Sc cloud is simulated based on the Second Dynamics and Chemistry of Marine Stratocumulus Field Study (DYCOMS-II) campaign (Stevens et al., 2003), with fixed surface fluxes, subsidence, and a simple parameterization for longwave radiative cooling (Ackerman et al., 2009). The model domain is  $3.2\text{ km} \times 3.2\text{ km} \times 2.56\text{ km}$  in  $x$ ,  $y$ , and  $z$  directions. We use a grid spacing of  $10\text{ m} \times 10\text{ m} \times 5\text{ m}$  to resolve the energy-containing eddies and the sharp thermodynamic gradients across the entrainment interface layer. Unresolved scalar inhomogeneity and turbulent mixing that control droplet response are represented by the coupled LEM (Hoffmann et al., 2019), which redistributes the particle-level supersaturation fluctuation  $S'$  at an effective vertical resolution of  $\Delta z_{\text{LEM}} = \Delta z_{\text{LES}}/n_p \approx 5\text{ cm}$  (see below). The model time step  $\delta t = 0.5\text{ s}$ , and the total model integration time is 5 h. The results are analyzed only for the last 2 h of the simulation.

The LCM particles, each representing the same number of hydrometeors, are initialized as sea-salt particles with dry radii randomly chosen from a log-normal distribution (geometric mean radius of  $r_{m,a} = 80\text{ nm}$ , geometric standard deviation  $\sigma_r = 1.4$ ). Initial aerosol number concentrations of  $N_a = 50, 100, \text{ and } 200\text{ cm}^{-3}$  are considered, named N50, N100, and N200, respectively. Results are discussed mainly for the N100 case unless otherwise stated. Note that droplet sedimentation and collision-coalescence processes are not considered, as we focus on the evolution of the DSD shape in non-drizzling stratocumulus. Given the absence of drizzle, the maximum droplet radii are approximately 15, 12, and  $9\text{ }\mu\text{m}$  for the N50, N100, and N200 cases, respectively. For droplets in the  $5\text{--}15\text{ }\mu\text{m}$  range, terminal fall speeds are  $\mathcal{O}(1\text{ cm s}^{-1})$  (Yau and Rogers, 1996), which is negligible compared to typical turbulent vertical-velocity fluctuations near cloud top (e.g.  $\sigma_w$  is  $\mathcal{O}(10^{-1}\text{ m s}^{-1})$ ; Wood, 2012). However, neglecting sedimentation may slightly alter

droplet residence times and hence microphysical exposure near cloud top.

The LEM further complements the high resolution of the LES. In the  $L^3$  model, the vertical LES grid spacing ( $\Delta z_{\text{LES}}$ ) and the number of LCM particles per grid box ( $n_p$ ) jointly determine the resolution of the LEM, defined as  $\Delta z_{\text{LEM}} = \Delta z_{\text{LES}}/n_p$ . In this simulation, we initialize 100 LCM particles per grid box, resulting in a  $\Delta z_{\text{LEM}}$  of approximately 5 cm, which allows the model to represent fine-scale scalar inhomogeneity relevant for inhomogeneous mixing in stratocumulus within the  $L^3$  framework (Hoffmann and Feingold, 2019).

## 2.3 Lagrangian Particle Tracking

To explicitly resolve the microphysical histories of individual droplets, we implemented a Lagrangian particle-tracking algorithm within the  $L^3$  model. Each LCM particle is assigned a unique identifier (ID) upon initialization, which is preserved throughout its lifecycle. For this study, we tracked 400 particles. At initialization, four distinct and equidistantly spaced vertical columns were selected across the domain. Within each column, one particle was randomly chosen from each of the lowest 100 vertical grid boxes, yielding 100 tracked particles per column. To manage data volume and focus exclusively on in-cloud evolution, we applied a conditional recording scheme: data were recorded only when a flagged particle resided within a grid box classified as cloudy ( $q_c \geq 0.01\text{ g kg}^{-1}$ ). We used the first 3 h as a spin-up period, during which the flagged particles were dispersed by boundary-layer turbulence and became nearly well mixed within the boundary layer. Particle output was then enabled, and the final 2 h are used for analysis (Sect. 2.2).

These tracked particles function as “virtual observers”, although they remain microphysically active, undergoing condensation and evaporation indistinguishable from the standard LCM particles. At each time step, they sample the local thermodynamic conditions and record the bulk microphysical statistics of the droplet ensemble within their resident grid cell. Since particles typically undergo multiple cycles of entrainment and detrainment driven by turbulent vertical circulations, they often re-enter the cloud layer several times. Consequently, the effective number of in-cloud records is larger than the number of tracked LCM particles.

The recorded dataset includes each particle's Lagrangian state vector (unique ID, radius  $r$ , multiplicity, supersaturation fluctuation  $S'$ , three-dimensional velocity components, and position) together with the co-located Eulerian state variables, including pressure  $p$ , turbulent kinetic energy dissipation rate  $\varepsilon$ , LES gridbox mean supersaturation  $\bar{S}$ , temperature  $T$ , and water vapor mixing ratio  $q_v$ . Additionally, properties derived from the full droplet population within the grid box, including  $q_c$ , cloud droplet number concentration  $N_c$ , supersaturation standard deviation  $\sigma_S$ ,  $r_m$ , and  $d_r$ , were calculated and stored alongside the particle data. This approach ensures

that the dataset captures the complete microphysical context of droplets, specifically during their residence in the cloud, filtering out the dry aerosol phase.

The resulting trajectories are recorded at a sampling interval equivalent to the model timestep ( $\delta t = 0.5$  s). To mitigate the high-frequency noise inherent to Lagrangian trajectories in turbulent flows, these properties were smoothed using a Gaussian kernel filter (Virtanen et al., 2020) with a window size of 10 s during post-processing.

### 3 Results

#### 3.1 Dynamical and Mixing Characteristics of the STBL

We begin by characterizing the dynamical and mixing structure of the STBL. Figure 1a shows the mean vertical profile of two moist-adiabatically conserved variables: total water mixing ratio ( $q_t$ ) and liquid water potential temperature ( $\theta_l$ ). The STBL consists of a well-mixed layer, characterized by high  $q_t$  and low  $\theta_l$ , the free troposphere with low  $q_t$  and high  $\theta_l$ , and an entrainment interface layer (EIL) in between. The EIL is characterized by sharp gradients in both moisture and temperature, typically within a few tens of meters. It represents the transition zone where turbulent eddies from the boundary layer mix with overlying dry and warm free-tropospheric air. Based on the sharp contrast in  $q_t$  and  $\theta_l$  between the boundary layer and the free troposphere, we adopt a mixing fraction,

$$\chi = \frac{(q_t - q_{t,bl})}{(q_{t,ft} - q_{t,bl})}, \quad (3)$$

which represents the fraction of free-tropospheric air mixed with boundary-layer air (Yang et al., 2016; Lu et al., 2018b). While calculating  $\chi$  using  $\theta_l$  yields results highly correlated with those based on  $q_t$ , we select  $q_t$  as the conserved variable because it exhibits a more constant profile in the free troposphere (Fig. 1a), making the choice of representative free-troposphere value easier.

In this simulation, the reference values  $q_{t,ft}$  and  $q_{t,bl}$  are set to their initial values of 1.5 and 9.5 g kg<sup>-1</sup>, respectively, which remain nearly constant throughout the simulation. Note that turbulent fluctuations can cause local parcels to exhibit  $q_t$  values exceeding the domain-averaged  $q_{t,bl}$ , resulting in slightly negative  $\chi$  values (accounting for  $\sim 0.02\%$  of the total data; Fig. 2). These minor deviations reflect the natural physical variability within the boundary layer reservoir.

At the top of the STBL, stable stratification inhibits mixing between the boundary layer and the free troposphere. Consequently,  $\chi$  is also strongly stratified (Fig. 1d), with the most rapid change confined to the EIL, identifying this region as the primary site of entrainment and mixing. The cloud top and EIL are persistently negatively buoyant (Fig. 1b), where the buoyancy is defined by

$$B = g \left( \frac{\theta_v - \bar{\theta}_v}{\bar{\theta}_v} \right) \quad (4)$$

where  $g$  is the gravitational acceleration, and  $\theta_v$  and  $\bar{\theta}_v$  are the local and horizontally averaged virtual potential temperatures, respectively. The negative  $B$  arises from evaporative cooling during entrainment and longwave radiative cooling (Stevens, 2002; Wood, 2012).

High values of  $\chi$  are rarely observed within the cloud interior. However, localized pockets of enhanced  $\chi$  can appear within the boundary layer, particularly near cloud holes and in descending branches of the STBL vertical circulation ( $W < 0$  m s<sup>-1</sup>, Fig. 1c). For example, at  $x = 0.2$  km and  $x = 3$  km, cloud holes coincide with downdrafts and elevated  $\chi$ , possibly indicating the accumulation of previously entrained dry air.

While  $\chi$  can highlight regions influenced by entrainment, its relationship with microphysical variables such as  $r_m$  and  $d_r$  is not straightforward. To explore this quantitatively, Fig. 2 illustrates the relationships between various variables and  $\chi$ .  $q_c$  is negatively correlated with  $\chi$ , with high  $q_c$  ( $> 0.5$  g kg<sup>-1</sup>) occurring only in regions with very low  $\chi$  ( $< 0.1$ ), corresponding to undiluted, nearly adiabatic cloud interiors. Notably, all panels show a dense cluster around  $\chi < 0.1$ , suggesting a prevalence of nearly adiabatic cloud interior during both ascent and descent (Fig. 2b). High values of  $\chi$  are associated with  $-1$  m s<sup>-1</sup>  $< W < 1$  m s<sup>-1</sup>, a range typically found in regions experiencing entrainment and mixing at the cloud top under near-neutral conditions.

Figures 2c and d show that  $r_m$  tends to decrease and  $d_r$  tends to increase with increasing  $\chi$  in regions that remain nearly adiabatic ( $\chi < 0.1$ ). However, when  $\chi > 0.1$ , the mean values flatten out, and the relationship becomes less clear: neither  $r_m$  nor  $d_r$  shows a strong or consistent dependence on  $\chi$ . This suggests that while  $\chi$  may correlate with microphysical variability in undiluted cloud regions, it alone cannot explain the droplet size evolution in environments influenced by entrainment and mixing. Therefore, to gain a more comprehensive understanding of the evolution of  $r_m$  and  $d_r$ , especially under the influence of entrainment and mixing, it is essential to consider the full growth history of individual droplets.

To illustrate this approach, Figs. 1 and 3 show an example particle trajectory that captures a representative pathway within the STBL vertical circulation. Droplets along this path undergo four key microphysical stages: (i) activation near the cloud base, (ii) condensational growth in updrafts, (iii) entrainment and mixing at the cloud top, and (iv) descent, evaporation, and deactivation. These stages leave clear imprints on the evolution of  $r_m$  and  $d_r$ . While both  $r_m$  and  $q_c$  generally increase with height in cloudy updrafts, a sharp decrease occurs near cloud holes (Fig. 3a and b), reflecting the effects of mixing and evaporation. In contrast,  $d_r$  shows a more complex distribution: it is typically lower inside clouds but increases near cloud top and cloud-hole boundaries (Fig. 3c), resembling the spatial structure of  $\chi$  (Fig. 1d). In the following sections, we examine how particle histories shape distinct DSD aging regimes and control the evolution of  $r_m$  and  $d_r$ .

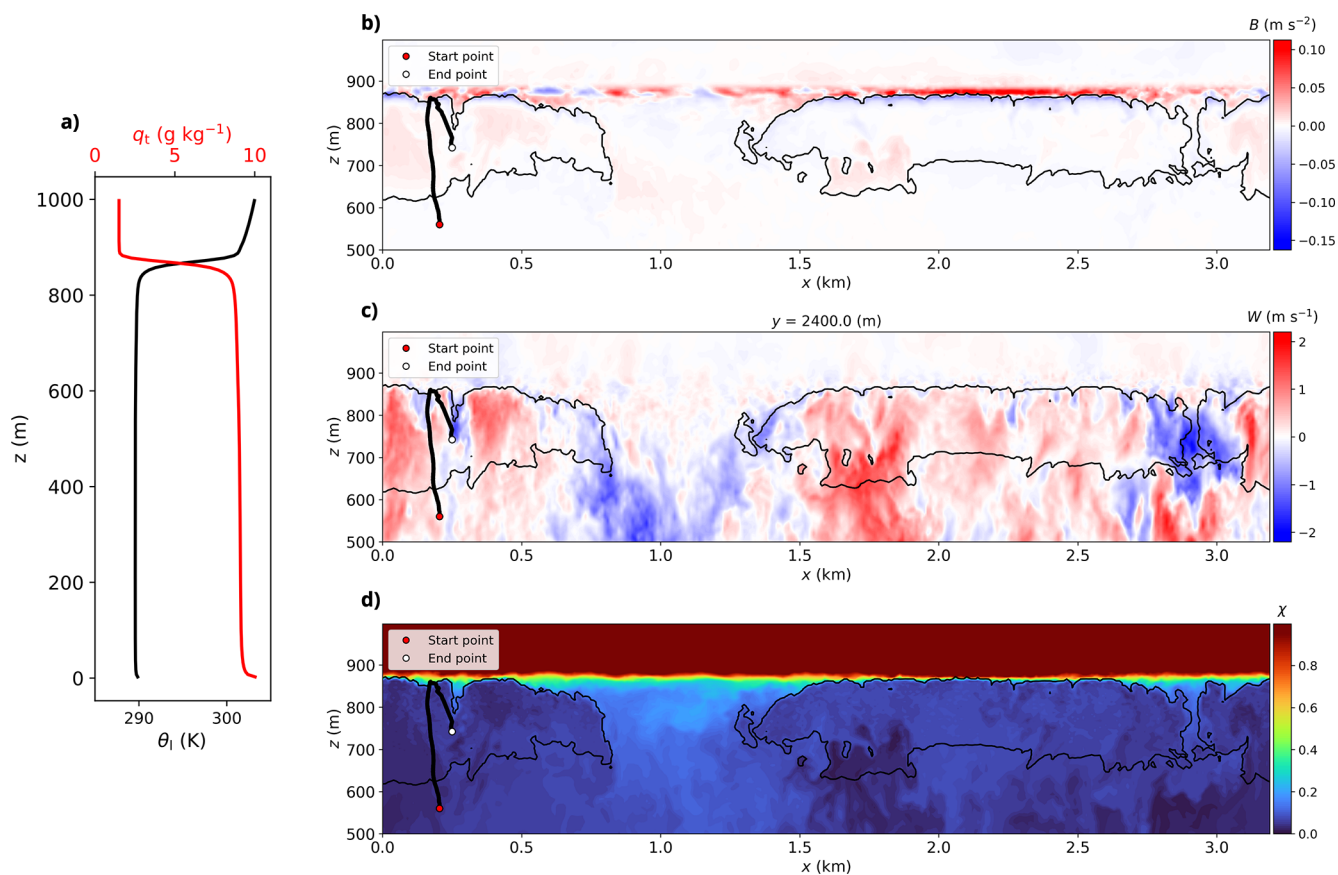


**Figure 1.** (a) Vertical profiles of  $q_t$  (red solid line) and  $\theta_1$  (black solid line). Vertical cross-sections of (b) buoyancy  $B$ , (c) vertical velocity  $W$ , and (d) mixing fraction  $\chi$  at  $y = 2400$  m, presented as a snapshot at a simulation time of  $t = 13320$  s. In panels (b–d), the Lagrangian trajectory of a selected particle is overlaid as a thick black line, tracing its path from the entry point (red dot at  $t = 12298.5$  s) to its current position (white dot at  $t = 13320$  s). The thin black solid lines indicate where the cloud water mixing ratio  $q_c = 0.01 \text{ g kg}^{-1}$ .

### 3.2 Droplet Evolution Pathways in the $r_m$ – $d_r$ Phase Space

To further understand the evolution of  $r_m$  and  $d_r$ , we analyze the droplet evolution in the  $r_m$ – $d_r$  phase space. Figure 4a shows the frequency distribution of the  $r_m$ – $d_r$  phase space obtained from three-dimensional model output, where  $r_m$  and  $d_r$  are estimated from cloud droplets with radii  $> 1 \mu\text{m}$  only. Overall, the range of  $d_r$  is inversely proportional to  $r_m$ , with  $d_r = 1.0$  at  $r_m = 3 \mu\text{m}$  and  $d_r \rightarrow 0$  for  $r_m = 12 \mu\text{m}$ . The high-frequency pattern visible in Fig. 4a is divided into two distinct parts, which can be constrained by  $S$  (Fig. 5). We define these as the “growth pathway” characterized by low  $d_r$  for  $S \geq 0$  and hence condensational growth (Fig. 5c and d), and the “evaporation pathway” characterized by high  $d_r$  for  $S < 0$  and hence evaporation (Fig. 5e and f). Thus, we expect a quasi-loop structure of droplet evolution from the growth pathway to the evaporation pathway. Figure 4b shows the LCM particle trajectories in this phase space, with black and green markers indicating the start and end points, respectively, and the corresponding frequency distribution in

Fig. 4c. Note that the high-density patterns resemble the two pathways identified in the model output frequency distribution (Fig. 4a). In this analysis, we treat each continuous in-cloud segment of a particle trajectory as an independent trajectory, as a single particle can enter the cloud multiple times. This results in a total of 384 trajectory segments. We confirm that the qualitative features of Fig. 4 and other analyses presented later in this study (e.g. Fig. 5) remain unchanged when using subsets of 100, 200, or 400 trajectories, indicating that the results are robust with respect to sample size throughout the analysis.

The growth pathway can be described by

$$d_r = d_{r,0} \frac{r_{m,0}^2}{r_m^2}, \quad (5)$$

following the analytic solution proposed by Liu et al. (2006), where  $d_{r,0}$  and  $r_{m,0}$  denote the boundary values. Here, we use  $d_{r,0} = 0.01$  and  $r_{m,0} = 12 \mu\text{m}$  to show Eq. (5) as a cyan dashed line in Fig. 4a and b.

While Eq. (5) effectively captures the growth pathway, it fails to describe the evaporation pathway (Fig. A1). To ap-

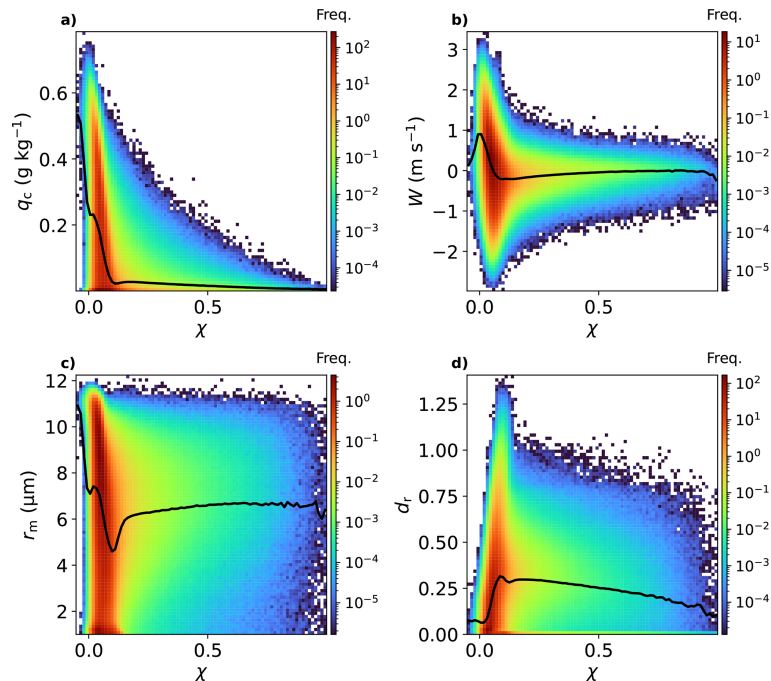


**Figure 2.** Two-dimensional density histograms of  $\chi$  vs. (a)  $q_c$ , (b)  $W$ , (c)  $r_m$ , and (d)  $d_r$ , with black solid lines indicating the mean of each variable in bins of  $\chi$ .

proximate the latter, we utilize percentile-based diagnostics, where the 50th, 75th, and 90th percentiles of  $d_r$  at each  $r_m$  bin provide a reasonable empirical representation of the evaporation pathway (Fig. 4a–c), exhibiting an inverse trend between  $d_r$  and  $r_m$ . In analogy to Eq. (5), the fitted function is given as

$$d_r = d_{r,\max} \left( 1 - \frac{r_m^2}{r_{m,\max}^2} \right), \quad (6)$$

where  $r_{m,\max}$  and  $d_{r,\max}$  denote the maximum values of  $r_m$  and  $d_r$ , respectively. Each percentile line (p50, p75, and p90) can be represented by a distinct  $d_{r,\max}$  value for the same  $r_m$  (e.g. Fig. 4a). For instance,  $d_r$  approaches zero as  $r_m$  approaches  $r_{m,\max}$ , whereas  $d_{r,\max}$  typically occurs at much smaller droplet sizes (e.g.  $r_m < 3 \mu\text{m}$ ), well below  $r_{m,\max}$ . A detailed discussion on this empirical formulation is provided in Sect. 4.

### 3.3 Different Regimes of Droplet Evolution Pathways

In the previous section, we showed that droplet evolution pathways diverge depending on whether droplets grow or decay. To better characterize these differences, we analyze the  $r_m$ – $d_r$  phase space in terms of the sign of the correlation between  $dd_r/dt$  and  $dr_m/dt$ . This analysis uses the particle trajectories shown in Fig. 4b and c.

As already indicated above, the resulting patterns are closely tied to the supersaturation  $S$ . As shown in Fig. 5a and b, the phase space structure under all  $S$  conditions can

be decomposed into two dominant subsets based on  $S \geq 0$  and  $S < 0$  (second and third rows). While the droplet life cycle is a continuous process, we can classify it into four distinct regimes, each characterized by a dominant set of microphysical processes: A (*activation*) and B (*adiabatic growth*) for  $S \geq 0$ , and C (*entrainment and descent*) and D (*deactivation*) for  $S < 0$ , each of which corresponds to a dominant microphysical process. Although precipitation is another key process in DSD evolution, we focus on condensational growth and evaporation, examining phase-space-averaged microphysical and environmental properties across the four regimes (Figs. 6 and 7).

#### 3.3.1 Activation Regime ( $S \geq 0$ )

In the *activation regime*, the  $dr_m/dt$ – $dd_r/dt$  correlation is primarily positive (region A in Fig. 5c and d), especially when  $r_m < 2 \mu\text{m}$ . This regime is associated with droplet activation occurring in updrafts (Fig. 7b) near the cloud base (Fig. 7c), as indicated by high net activation rates (Fig. 6i). The corresponding increase in droplet number concentration (Fig. 6c) marks cloud formation. In Fig. 4b, most particle trajectories initiate within this regime (black dots). During this phase, condensational growth increases  $r_m$ , while the time-dependent activation of aerosols with different critical supersaturations leads to an increase in  $d_r$ . This results in a transient broadening of the DSD, prior to narrowing due to subsequent condensational growth.

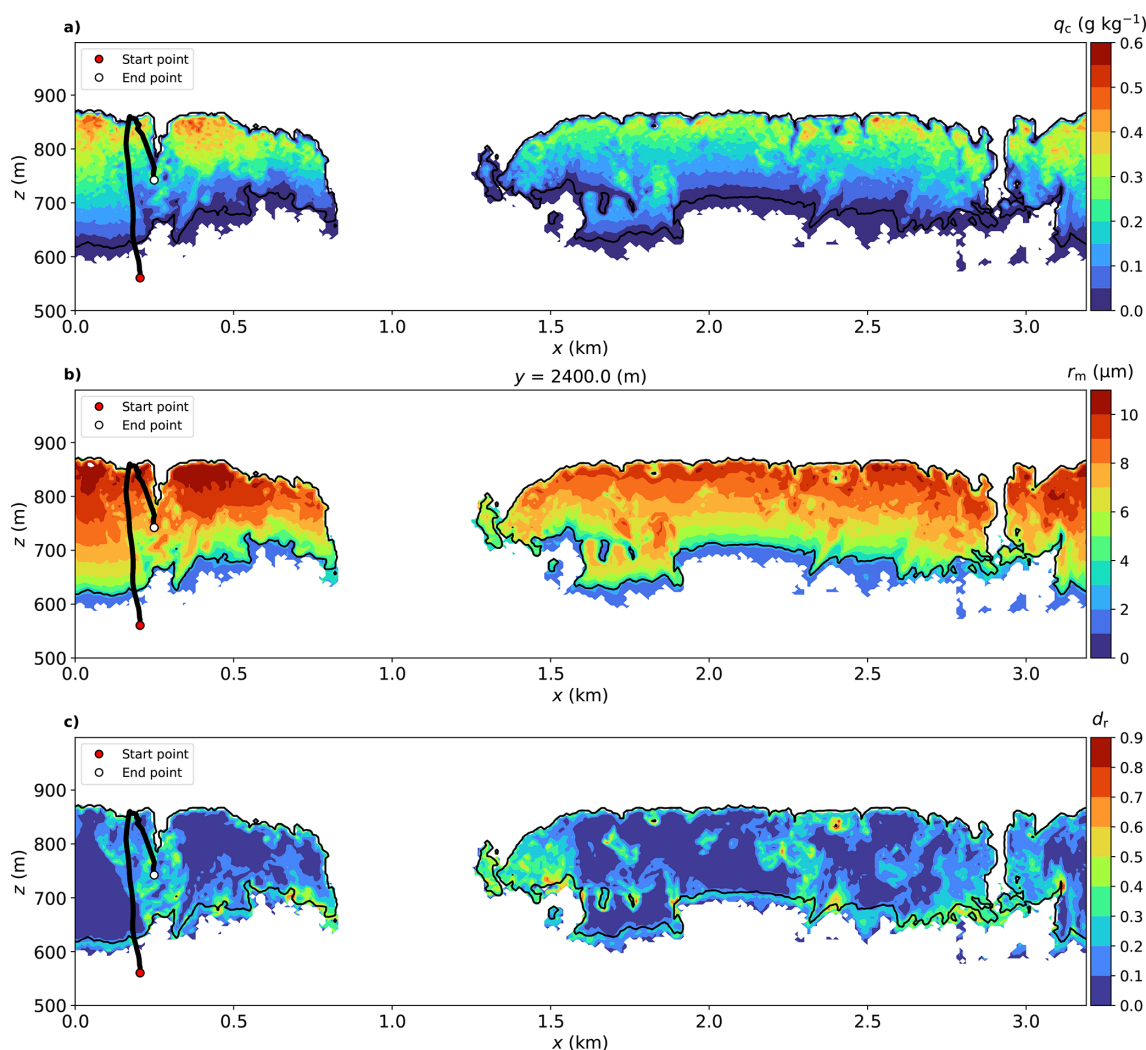


**Figure 3.** Vertical cross-sections of (a)  $q_c$ , (b)  $r_m$ , and (c)  $d_r$  at  $y = 2400$  m, presented as a snapshot at a simulation time of  $t = 13320$  s. The thick black line traces the Lagrangian history of a selected droplet, ending at its current position (white dot) at this instant and extending backward in time to its cloud entry point (red dot). The thin black lines in each panel indicate the cloud boundary defined by a mixing ratio of  $q_c = 0.01$  g kg<sup>-1</sup>.

### 3.3.2 Adiabatic Growth Regime ( $S \geq 0$ )

Following the *activation regime*, droplets enter the *adiabatic growth regime* (region B in Fig. 5c and d), particularly when  $d_r < 0.1$ . In this regime, cloud droplets grow by condensation within regions of high supersaturation (Fig. 6g), strong updrafts (Fig. 7b), and low mixing fraction  $\chi$  (Fig. 6h). Activation and deactivation are negligible (Fig. 6i), resulting in an almost constant droplet number concentration,  $N_c$  (Fig. 6c). The turbulent kinetic energy dissipation rate ( $\varepsilon$ ) remains low (Fig. 7g), indicating weak turbulence. In addition, the small standard deviation of supersaturation,  $\sigma_S$  (Fig. 7h), indicates a highly homogeneous supersaturation field, implying minimal entrainment and mixing-driven dilution of the cloudy air.

In this regime, the rates of change of  $r_m$  ( $dr_m/dt$ ) and  $d_r$  ( $dd_r/dt$ ) exhibit a negative correlation, reflecting classical condensational growth behavior: the radius of small droplets grows faster, narrowing the DSD as its mean size increases. This behavior aligns with parcel theory and is typically observed within the adiabatic cores of stratocumulus clouds (Yau and Rogers, 1996; Liu et al., 2006).

### 3.3.3 Entrainment and Descent Regime ( $S < 0$ )

After the *adiabatic growth regime*, droplets enter the *entrainment and descent regime* (region C in Fig. 5e and f). In this regime, the  $dr_m/dt$ – $dd_r/dt$  correlation becomes negative:  $r_m$  decreases and  $d_r$  increases due to evaporation caused either by mixing with entrained free-tropospheric air or by adiabatic heating during descent. Unlike in the previous

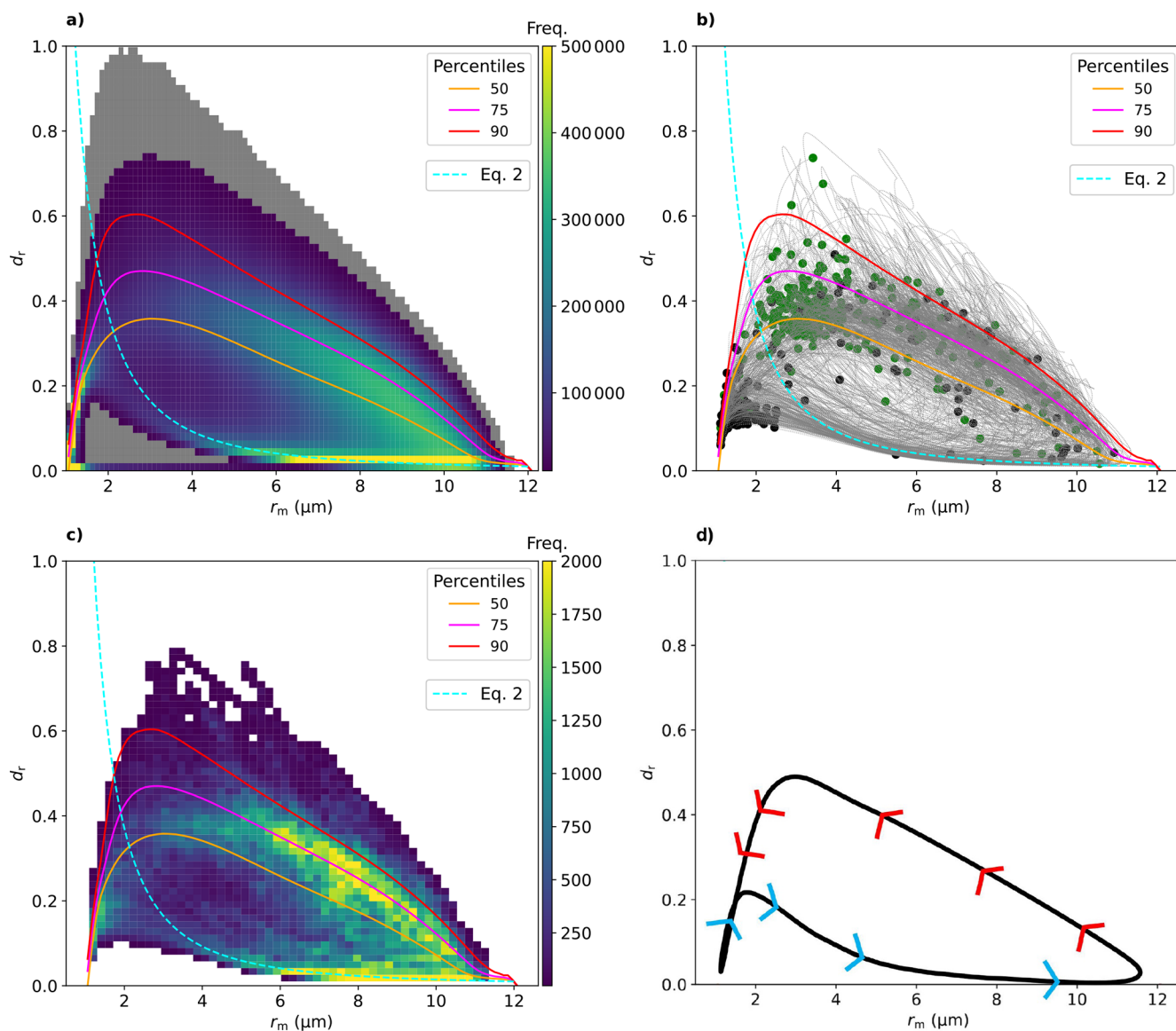


**Figure 4.** (a) Two-dimensional frequency histogram in  $r_m$  and  $d_r$  phase space. (b) Corresponding droplet evolution pathways (gray dotted lines) with start/end points in black/green. (c) The corresponding frequency distribution of droplet evolution pathways. (d) Conceptual schematic summarizing the composite evolution loop, constructed from the most frequently observed trajectory patterns in the  $r_m$ – $d_r$  phase space. Blue and red arrows represent the dominant directions of growing and decaying pathways, respectively, based on the Lagrangian trajectory. In each panel, 50th, 75th, and 90th percentiles at each  $r_m$  value and Eq. (5) are indicated as solid lines in orange, magenta, red, and cyan, respectively. In panel (a), the gray-shaded regions indicate areas where the sample count is below 10 000, which are masked for statistical robustness.

regimes, where most droplets follow similar evolution pathways, droplet pathways diverge significantly in this regime (Fig. 4b). Notably, for rare cases of very high  $d_r$ ,  $r_m$  increases while  $d_r$  decreases (Fig. 5e and f). These represent cases of narrowing mixing (Lim and Hoffmann, 2023), wherein an extremely wide DSD narrows after mixing due to the substantial evaporation of small droplets, causing the average droplet size to increase.

While some droplets experience rapid altitude changes, following the STBL vertical circulation (indicated by the p50 line in Fig. 4), others remain near the cloud top, close to the p90 line (Fig. 7f). These latter droplets exhibit weak vertical velocity  $W$  (Fig. 7e) within negatively buoyant air (Fig. 7d) and are subject to stronger entrainment-driven dilution. This is indicated by high  $\varepsilon$  (Fig. 7j), high  $\sigma_S$  (Fig. 7k), low  $S$  (Fig. 6j), and high  $\chi$  (Fig. 6k). Consequently, droplets in more diluted regions (near the p90 line in Fig. 6k) undergo

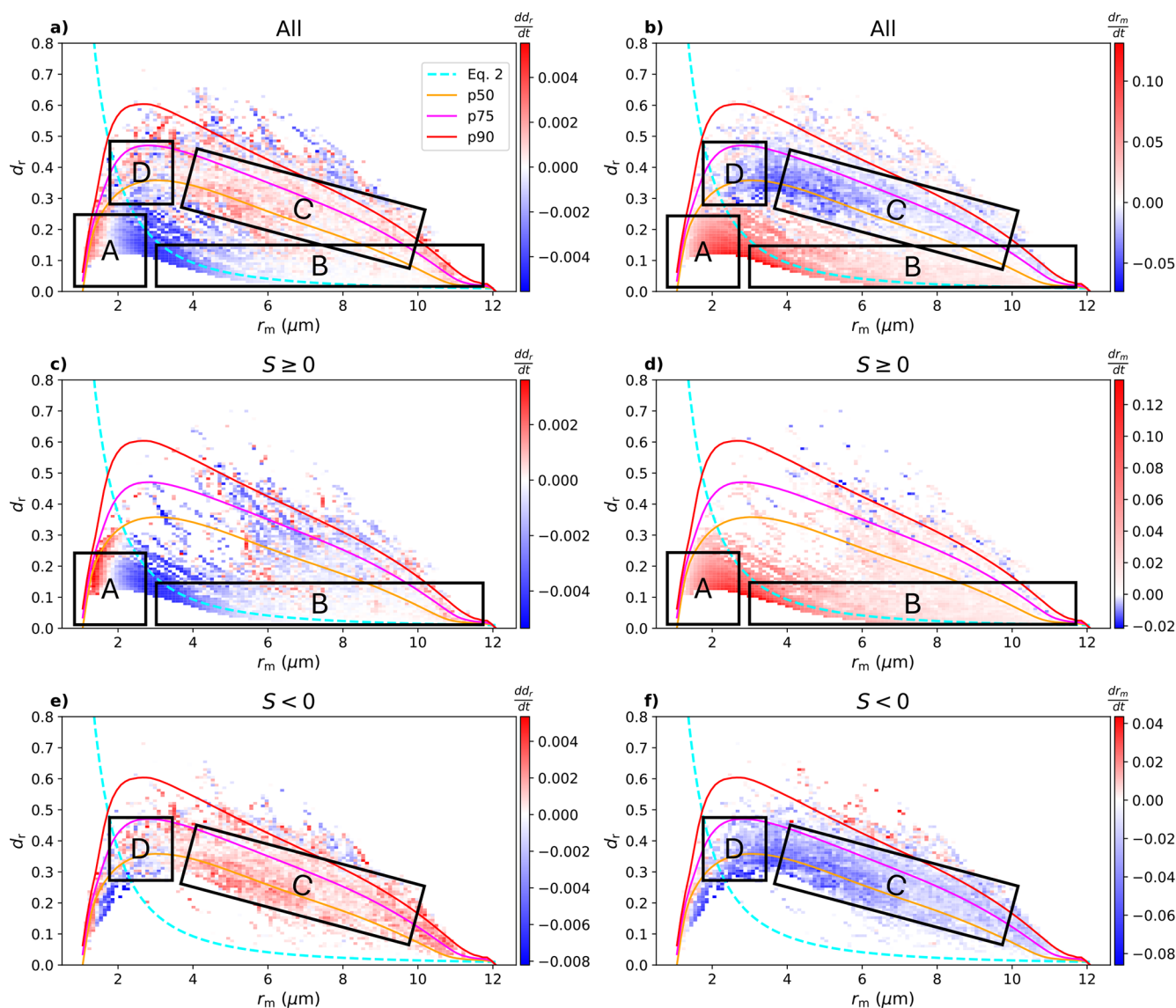


**Figure 5.** Two-dimensional binned mean values of the rates of change,  $dd_r/dt$  (first column) and  $dr_m/dt$  (second column), in the  $r_m$ – $d_r$  phase space for all conditions (first row),  $S \geq 0$  (second row), and  $S < 0$  (third row). In each panel, the 50th, 75th, and 90th percentile values (p50, p75, p90), and Eq. (5) from Fig. 4 are indicated by solid lines in orange, magenta, red, and cyan, respectively. Each panel shows 2D binned mean values of  $dd_r/dt$  and  $dr_m/dt$  in the  $r_m$ – $d_r$  phase space, based on Lagrangian trajectories smoothed with a Gaussian kernel (window = 10 s) and averaged over time.

more abrupt evaporation and deactivation (Fig. 6l) compared to those following the STBL vertical circulation (near the p50 line in Fig. 4b), which experience more gradual evaporation (Fig. 7l) and lower  $\chi$  (Fig. 6k).

To determine whether certain droplets escape the strong effects of entrainment and mixing (i.e. those following the downdrafts of the STBL vertical circulation with minimal dilution), we analyze the density distribution of maximum  $\chi$  values along individual droplet trajectories (Fig. 8). The maximum  $\chi$ , calculated over each droplet's lifetime from activation to deactivation, serves as a proxy for the droplet's entrainment history, representing the maximum fraction of en-

vironmental air the parcel has experienced. Trajectories with a maximum  $\chi < 0.1$  indicate a relatively minor impact from entrainment. As shown in Fig. 8, a notable fraction of parcels exhibit low maximum  $\chi$  values, suggesting that these are not substantially diluted by entrainment and mixing events near the cloud top. This is consistent with Fig. 4, where some droplets descend without a significant decrease in supersaturation  $S$  or increase in  $\chi$  (Fig. 6j and k) despite strong downdrafts (Fig. 7e).

The diversity of pathways in the evaporation regime contrasts with the *adiabatic growth* regime, where droplets follow nearly uniform growth paths. In the *entrainment and de-*

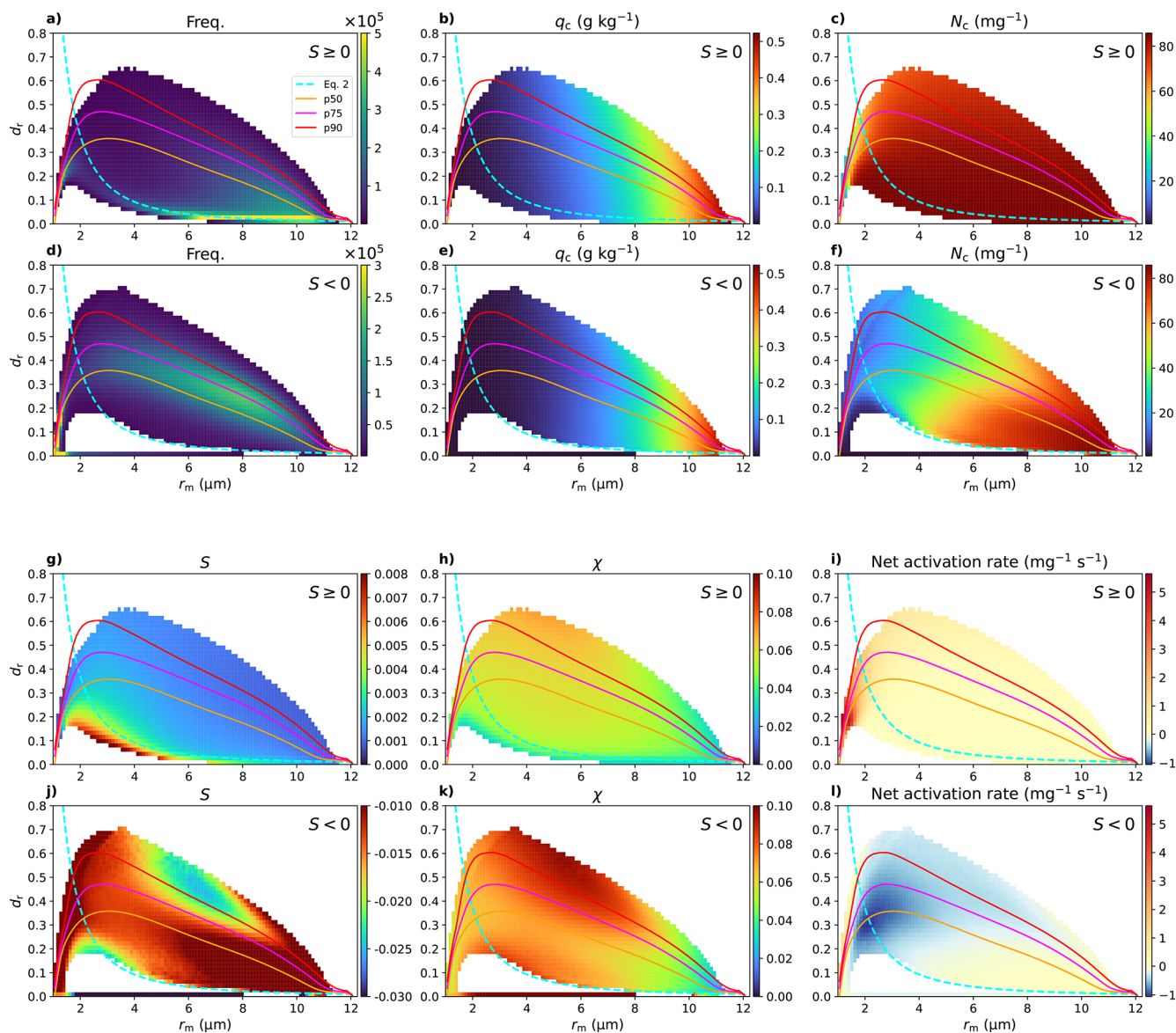


**Figure 6.** Two-dimensional binned mean values of cloud properties in the  $r_m$  and  $d_r$  phase space for  $S \geq 0$  (first and third row) and  $S < 0$  (second and fourth row). (a) and (d) show the frequency distributions, (b) and (e) show cloud water mixing ratio ( $q_c$ ), (c) and (f) show cloud droplet number concentration ( $N_c$ ), (g) and (j) show the mean supersaturation ( $S$ ), (h) and (k) show mixing fraction ( $\chi$ ) and (i) and (l) show net activation rate (activation rate – deactivation rate). In each panel, the 50th, 75th, and 90th percentile values (p50, p75, p90), and Eq. (5) from Fig. 4 are indicated by solid lines in orange, magenta, red, and cyan, respectively. Values represent bin-averaged means from 3D simulation results during the final 2 h of simulation, mapped onto the  $r_m$ – $d_r$  phase space.

*scent* regime, trajectories diverge: some parcels are strongly diluted by entrainment (near the p90 line in Fig. 7e), while others experience minimal dilution, following the strong downdraft circulation (near the p50 line in Fig. 7e). To better understand the evolution of these diverse pathways and how microphysical properties diverge, we show changes in mixing-related properties for individual particle trajectories in the  $\chi$ – $z$  phase space (Figs. 9 and 10). We categorized droplets based on the 25th ( $\chi = 0.08$ ) and 75th ( $\chi = 0.14$ ) percentiles of their maximum lifetime  $\chi$  values (Fig. 8).

Droplets within parcels subject to strong entrainment-driven dilution experience high maximum  $\chi > 0.14$  (first row), while the second and third rows show droplets with intermediate ( $0.08 \leq \chi \leq 0.14$ ) and low ( $\chi < 0.08$ ) maximum values, respectively. In all cases,  $d_r$  remains below 0.1 during ascent and increases when  $W < 0$ , particularly for parcels with higher  $\chi$  (Fig. 9c, f, and i).

While most droplets descend without experiencing a substantial decrease in  $S$ , only a fraction are strongly diluted by entrainment, where  $S$  decreases as  $\chi$  increases (Fig. 10e).

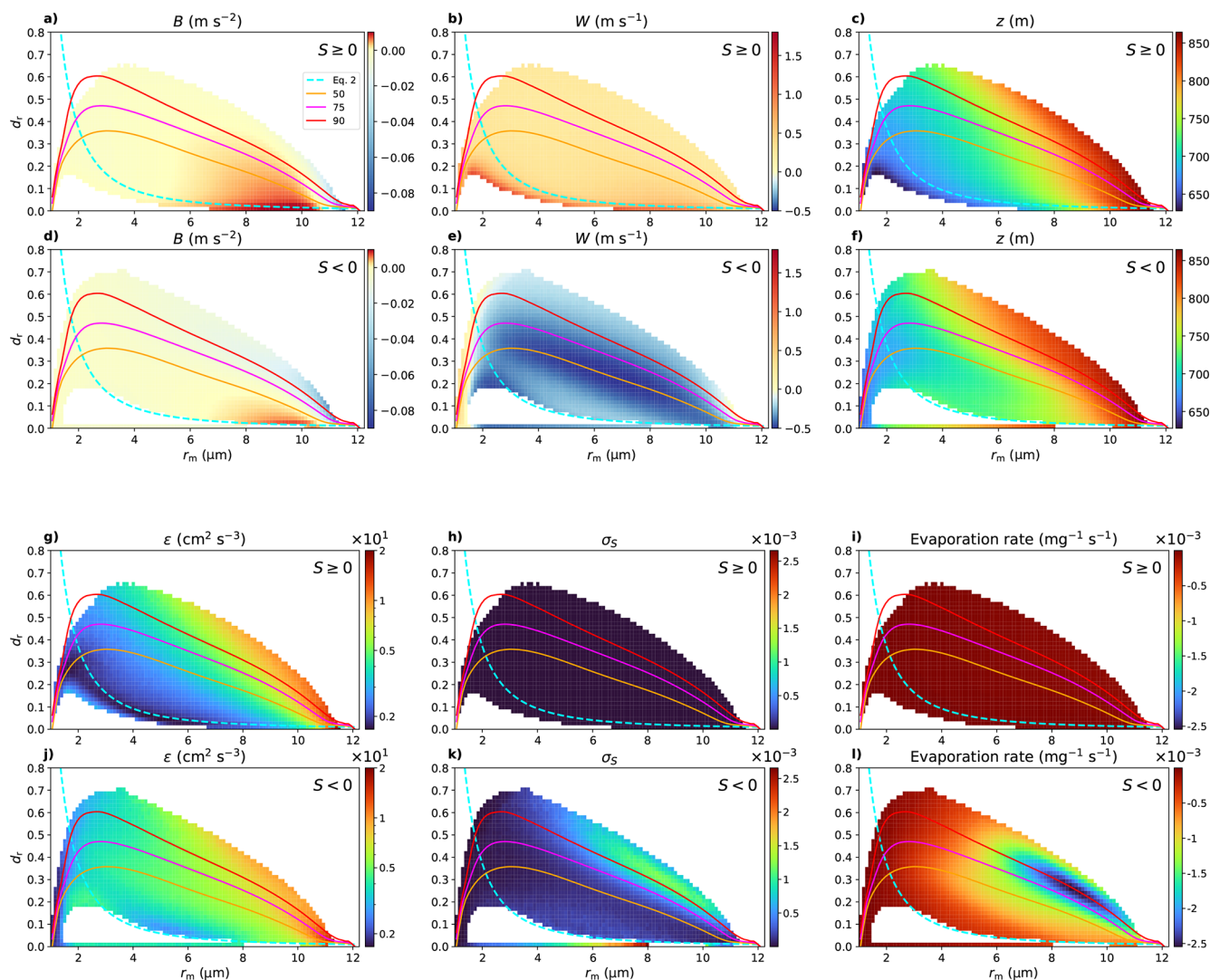


**Figure 7.** Two-dimensional binned mean values of cloud properties in the  $r_m$  and  $d_r$  phase space for  $S \geq 0$  (first and third row) and  $S < 0$  (second and fourth row). (a) and (d) show buoyancy ( $B$ ), (b) and (e) show vertical velocity ( $W$ ), (c) and (f) show height ( $z$ ), (g) and (j) show kinetic dissipation rate ( $\varepsilon$ ), (h) and (k) show supersaturation fluctuation ( $\sigma_S$ ) and (i) and (l) show the evaporation rate. In each panel, the 50th, 75th, and 90th percentile values ( $p_{50}$ ,  $p_{75}$ ,  $p_{90}$ ), and Eq. (5) from Fig. 4 are indicated by solid lines in orange, magenta, red, and cyan, respectively. Values represent bin-averaged means from 3D simulation results during the final 2 h of simulation, mapped onto the  $r_m$ – $d_r$  phase space.

For these droplets,  $S$  increases and  $\chi$  decreases again after reaching its peak, indicating the restoration of  $S$  following turbulent mixing and evaporation, as well as further homogenization within the cloud. Notably, supersaturation fluctuation ( $\sigma_S$ ) reaches a maximum at the cloud top while  $\chi$  increases, further indicating entrainment and mixing. As  $r_m$  decreases and  $d_r$  increases rapidly during mixing and evaporation (Fig. 9b and c), these droplets descend and evaporate in a new state characterized by modified  $r_m$  and  $d_r$ . Conversely, droplets that do not experience high  $\chi$  descend with a continuous state obtained at the end of the *adiabatic growth regime*, characterized by maximum  $r_m$  and minimum  $d_r$  (Fig. 9h and i).

Thus, for droplets within parcels subject to minimal dilution,  $r_m$  is primarily a function of altitude (Fig. 9h). At the same altitude,  $r_m$  is only slightly smaller at higher  $\chi$ , regardless of whether the droplets are ascending or descending (Fig. 9g). Meanwhile,  $d_r$  is larger during descent (Fig. 9i), reflecting the broadening of the droplet size distribution due to evaporation in the absence of the collision-coalescence process. Along these trajectories,  $S$  remains high, while  $\chi$  and  $\sigma_S$  remain low, suggesting that these droplets likely ascend and descend with negligible influence from entrainment. Furthermore, while both droplet groups undergo evaporation during descent, their initial  $r_m$  and  $d_r$  differ based on whether

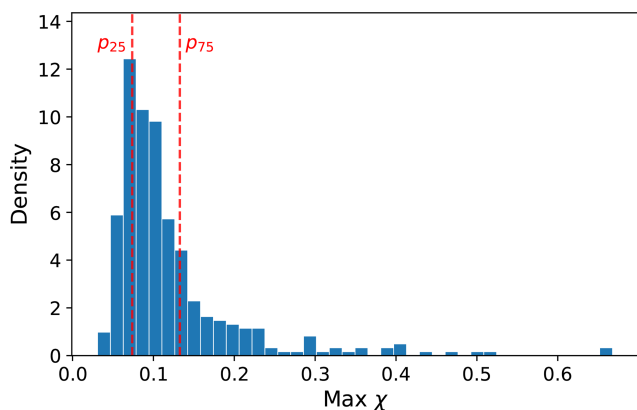


**Figure 8.** Density distribution of maximum  $\chi$  for individual tracked particles over their lifetime in the stratocumulus-topped boundary layer. The 25th ( $p_{25}$ ) and 75th ( $p_{75}$ ) percentiles of the maximum  $\chi$  are indicated with red dashed lines.

they reached a new state after mixing. This divergence leads to distinct evolution paths in the  $r_m$ – $d_r$  phase space.

Another difference between the ascending and descending pathways is the evolution of droplet number concentration. To separate the decrease in  $N_c$  caused by simple entrainment dilution from that caused by mixing-induced evaporation, we examine the dilution-corrected number concentration, defined as  $N_{ad} = N_c/(1 - \chi)$ . Here, the subscript “ad” denotes the adiabatic value, representing the concentration expected in an undiluted parcel. Specifically,  $N_{ad}$  is substantially lower at higher altitudes when parcels are strongly diluted by entrainment (Fig. 10a) compared to those experiencing minimal dilution (Fig. 10g). This distinct reduction is also evident in the  $r_m$ – $d_r$  phase space, where parcels subject to strong entrainment-driven dilution exhibit a rapid decrease in  $N_{ad}$  (Fig. 10a). This decrease, representing droplet loss beyond simple dilution, is consistent with inhomogeneous mixing, wherein some droplets completely evaporate in locally subsaturated environments while others remain relatively unaltered. The localized increase in  $\sigma_S$  further supports the conclusion that SGS supersaturation variability, as resolved by the LEM, drives this selective evaporation. These findings align with recent observational studies suggesting that inhomogeneous mixing signals are prevalent near the top of Sc clouds (Yeom et al., 2021).

However, we cannot ensure that  $N_c/(1 - \chi)$  has fully isolated the effects of evaporation from entrainment-driven dilution. While the spatial distribution of the mixing signal indicates stronger inhomogeneous characteristics near the cloud top and homogeneous-like features below, it is questionable whether changes observed in the lower cloud should be interpreted as a result of active entrainment, especially since the majority of parcels descending with the STBL vertical circulation experience minimal dilution through entrainment. These uncertainties highlight a fundamental ambiguity in interpreting in situ observations of  $r_m$  and  $N_c$  as indicators of

mixing type, particularly when a precise estimation of  $\chi$  is unavailable.

To resolve this ambiguity, the maps of  $Da_{\text{phase}}$ ,  $Da_{\text{evap}}$ , and the ratio  $\tau_{\text{phase}}/\tau_{\text{evap}}$  in the  $\chi$ – $z$  phase space (Fig. 11) quantify the varying inhomogeneous and homogeneous mixing signals at the same height. Here, the Damköhler number is defined generally as

$$Da = \frac{\tau_{\text{mix}}}{\tau_{\text{micro}}}, \quad (7)$$

where the mixing timescale (Baker and Latham, 1979; Baker et al., 1980) is

$$\tau_{\text{mix}} = \left(\frac{l^2}{\varepsilon}\right)^{\frac{1}{3}}. \quad (8)$$

Here,  $l$  represents the length scale of scalar inhomogeneity caused by entrainment, which breaks down to the Kolmogorov length scale through turbulent motion. Since the entrainment length scale  $l$  varies with the size of the entrained blobs, we estimate the mixing length using  $\chi$  as  $l = (\chi \cdot \Delta x \cdot \Delta y \cdot \Delta z)^{1/3}$ . Notably, using the equivalent geometric LES grid lengthscale ( $\approx 7.9$  m) as a proxy for  $l$  results in a larger  $\tau_{\text{mix}}$  but does not alter the conclusions. The relevant microphysical timescales are the phase relaxation time

$$\tau_{\text{phase}} = \frac{1}{4\pi D_v r_m N_c} \quad (9)$$

and the evaporation timescale

$$\tau_{\text{evap}} = -\frac{r_m^2}{2GS}, \quad (10)$$

defined only in subsaturated regions with  $S < 0$  (Squires, 1952; Lehmann et al., 2009; Tölle and Krueger, 2014). Here,  $D_v$  is the molecular diffusion coefficient for water vapor, and  $G = (F_d + F_k)^{-1}$  is the condensational growth parameter that summarizes the effects of vapor diffusion and heat conduction on condensation, with  $F_d$ , a coefficient associated with vapor diffusion, and  $F_k$ , associated with heat conduction (Yau and Rogers, 1996). Theoretically, when  $Da \gg 1$ , turbulent mixing is slower than the microphysical response, favoring inhomogeneous mixing. Conversely, when  $Da \ll 1$ , turbulent mixing is fast enough to homogenize the subsaturated entrained air with the saturated cloud air before droplets respond, leading to homogeneous mixing.

While mixing scenarios have often been characterized using a single Damköhler number constructed from one microphysical response time (e.g. Baker et al., 1980; Burnet and Brenguier, 2007), recent work has highlighted the limitations of such single-parameter descriptions and the need to consider multiple thermodynamic timescales (Lehmann et al., 2009; Jeffery, 2007; Lu et al., 2018a; Fries et al., 2021). Therefore, we define two Damköhler numbers:

$$Da_{\text{phase}} = \frac{\tau_{\text{mix}}}{\tau_{\text{phase}}} \quad \text{and} \quad Da_{\text{evap}} = \frac{\tau_{\text{mix}}}{\tau_{\text{evap}}}, \quad (11)$$

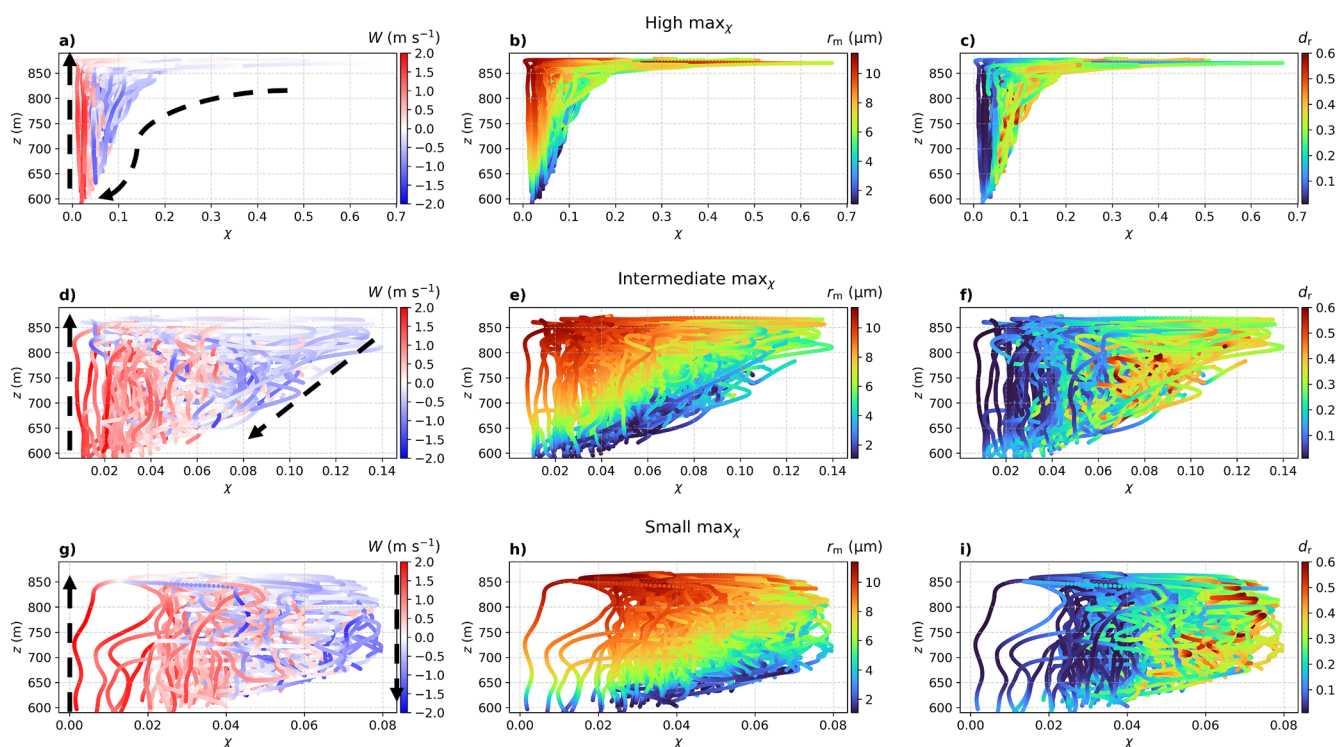


**Figure 9.** Particle trajectories in the  $\chi$ - $z$  phase space, where different colors of dots indicate: the  $W$  (first column),  $r_m$  (second column),  $d_r$  (third column). The first row shows trajectories with the maximum  $\chi > 0.14$ , the third row shows trajectories where the maximum  $\chi \leq 0.08$ , and the second row shows trajectories with intermediate values, where the maximum  $\chi$  lies between these two conditions. In panels (a), (d), and (g), the dashed black arrows indicate inferred droplet motion directions based on the vertical velocity  $W$ .

which represent the supersaturation relaxation-based and evaporation-based Damköhler numbers, respectively. Here,  $Da_{\text{phase}}$  measures how efficiently phase relaxation can restore supersaturation relative to turbulent mixing, whereas  $Da_{\text{evap}}$  measures how efficiently droplets can evaporate before the mixed air is re-saturated. In addition, we use the ratio between the two Damköhler numbers,  $\tau_{\text{phase}}/\tau_{\text{evap}}$ , which is closely related to the parameter suggested by Fries et al. (2021) and corresponds to the potential evaporation parameter of Pinsky et al. (2016).

In the high- $\chi$  regime (first row of Fig. 11), parcels subject to strong entrainment-driven dilution frequently exhibit  $Da_{\text{phase}} > 1$  (Fig. 11a) and  $Da_{\text{evap}} > 1$  (Fig. 11b), alongside a ratio of  $\tau_{\text{phase}}/\tau_{\text{evap}} \gtrsim 1$  (Fig. 11c). This combination is consistent with an inhomogeneous mixing scenario, in which a subset of droplets evaporates completely while the remaining droplets maintain a relatively large  $r_m$ . As these parcels descend,  $Da_{\text{phase}}$  tends to decrease (Fig. 11a), whereas  $Da_{\text{evap}}$  remains greater than unity (Fig. 11b). Consequently, reliance on  $Da_{\text{phase}}$  alone might falsely indicate a transition toward homogeneous mixing during descent. The persistently high  $Da_{\text{evap}}$ , however, contradicts this interpretation. These parcels retain the signature of inhomogeneous mixing (depleted  $N_c$ , high  $Da_{\text{evap}}$ ) well below the cloud top, even as a consistent decrease in  $\chi$  indicates no further active

entrainment dilution but mixing with boundary layer air. This occurs because they descend through air that remains incompletely homogenized, creating an environment more subsaturated than would be expected from adiabatic descent alone.

In contrast, trajectories that remain in the low- $\chi$  regime throughout their lifetime (third row of Fig. 11) tend to occupy regions with smaller  $Da_{\text{evap}}$  (Fig. 11h) but relatively large  $Da_{\text{phase}}$  (Fig. 11g), and with  $\tau_{\text{phase}}/\tau_{\text{evap}} < 1$  (Fig. 11i). In this regime, phase relaxation is fast compared to both turbulent mixing and evaporation. This implies that adiabatic warming during descent is the primary source of droplet evaporation, without additional subsaturation caused by entrainment and dilution. These signatures are consistent with a homogeneous mixing-like response during descent, in which droplets gradually adjust  $r_m$  under a comparatively uniform supersaturation field without a substantial decrease in  $N_c$ , aside from weak entrainment-driven dilution at the cloud top. Moreover, as  $\chi$  generally decreases during the descent, this implies no further strong effect of entrainment dilution during the descent. Crucially, this implies that the homogeneous-mixing-like signature often observed deeper in the cloud is not necessarily due to active entrainment and mixing at that level. Instead, it reflects droplet evaporation in weakly diluted, near-adiabatic parcels descending via the STBL vertical circulation (Telford and Chai, 1980; Wang et al., 2009).

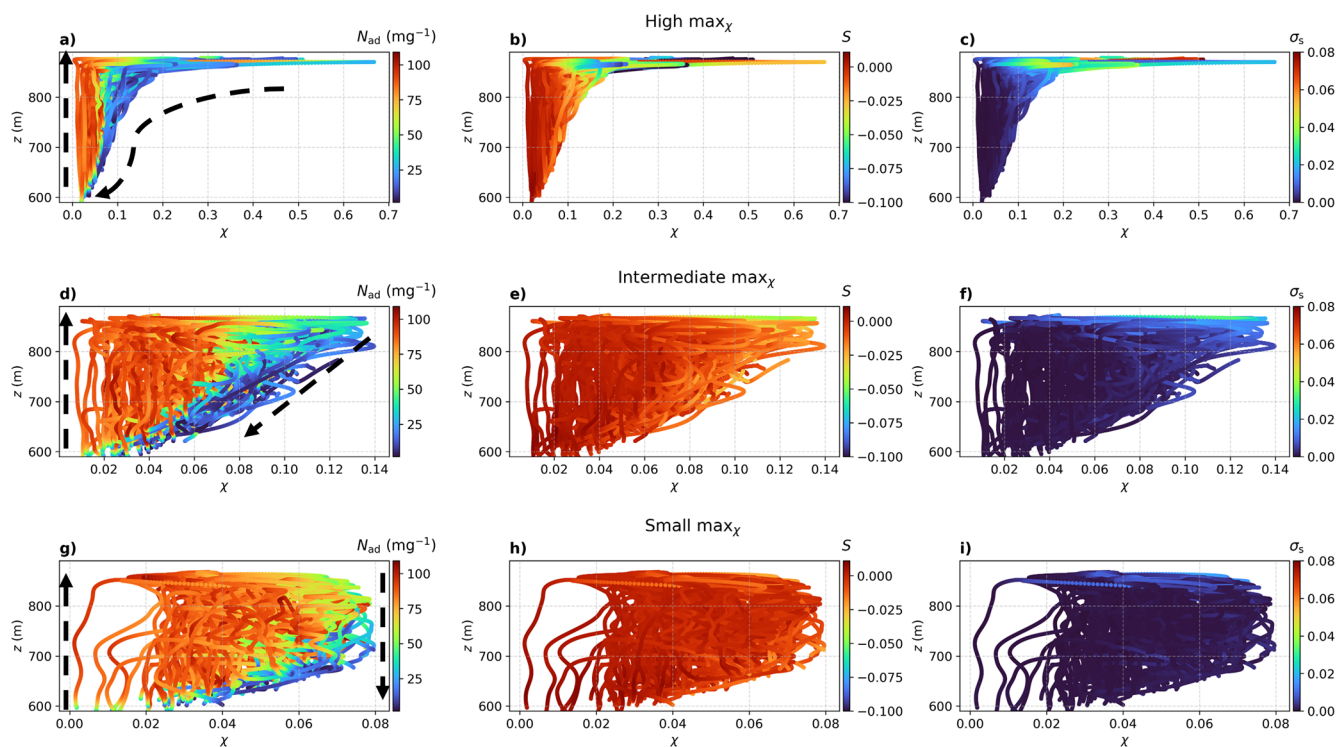


**Figure 10.** Particle trajectories in the  $\chi$ – $z$  phase space, where different colors of dots indicate: the  $N_{\text{ad}}$  (first column),  $S$  (second column), and  $\sigma_s$  (third column). The first row shows trajectories with the maximum  $\chi > 0.14$ , the third row shows trajectories where the maximum  $\chi \leq 0.08$ , and the second row shows trajectories with intermediate values, where the maximum  $\chi$  lies between these two conditions. In panels (a), (d), and (g), the dashed black arrows indicate inferred droplet motion directions based on the vertical velocity  $W$ .

The corresponding maps of the absolute timescales  $\tau_{\text{mix}}$ ,  $\tau_{\text{phase}}$ , and  $\tau_{\text{evap}}$  (Fig. 12) clarify why these diagnostics separate the regimes. The mixing timescale  $\tau_{\text{mix}}$  varies relatively modestly across the  $\chi$ – $z$  phase space (Fig. 12a and g), whereas  $\tau_{\text{phase}}$  and  $\tau_{\text{evap}}$  exhibit much stronger spatial contrasts. Therefore, changes in  $Da_{\text{phase}}$  and  $Da_{\text{evap}}$  are driven mainly by the two microphysical timescales. The phase relaxation time  $\tau_{\text{phase}}$  is strongly related to  $N_c$ : regions with strongly reduced  $N_c$  after complete evaporation events exhibit larger  $\tau_{\text{phase}}$  (Fig. 12b), while most other regions show much shorter  $\tau_{\text{phase}}$  (Fig. 12h). The evaporation timescale  $\tau_{\text{evap}}$  behaves inversely, being large in nearly saturated regions and decreasing rapidly with increasing subsaturation (Fig. 12c and i). Consequently, the ratio  $\tau_{\text{phase}}/\tau_{\text{evap}}$  serves as a direct indicator of where complete droplet evaporation is likely. This ratio is significantly higher for high maximum- $\chi$  parcels, reflecting their tendency toward complete evaporation, and remains much lower for low maximum- $\chi$  parcels until they reach the cloud base. Taken together, using  $\tau_{\text{phase}}/\tau_{\text{evap}}$  provides a natural separation between regimes where droplets are prone to complete evaporation due to entrainment-induced dilution and regimes where supersaturation is restored quickly enough to prevent substantial droplet loss.

These results highlight a contrast based on Lagrangian history. Parcels strongly diluted by entrainment near the cloud top are dominated by the inhomogeneous mixing signature. During descent, these parcels undergo gradual evaporation by adiabatic warming. Because of their greater subsaturation and decreased  $N_c$ , the droplets evaporate completely at a higher location in the cloud (Figs. 6l and 7f). Conversely, weakly diluted parcels descending near-adiabatically via the STBL circulation show a homogeneous-mixing-like signature driven solely by evaporation in the adiabatically descending parcel, rather than by active mixing events. These distinct Lagrangian histories explain why snapshots of  $r_m$  and  $N_c$  at a given altitude can simultaneously contain the imprints of both inhomogeneous and homogeneous mixing signatures, even without active entrainment events.

### 3.3.4 Deactivation Regime ( $S < 0$ )

Droplets transition into the *deactivation regime* at the end of their life cycle near the cloud base (Fig. 7f). In this regime, the relationship between  $dr_m/dt$  and  $dd_r/dt$  is complex, as  $r_m$  decreases while  $d_r$  increases for larger  $r_m$ , but decreases for smaller  $r_m$ . The decrease in  $r_m$  is due to the evaporation of droplets. For larger  $r_m$ ,  $d_r$  initially increases, as observed in the *entrainment and descent* regime. However, as the droplets

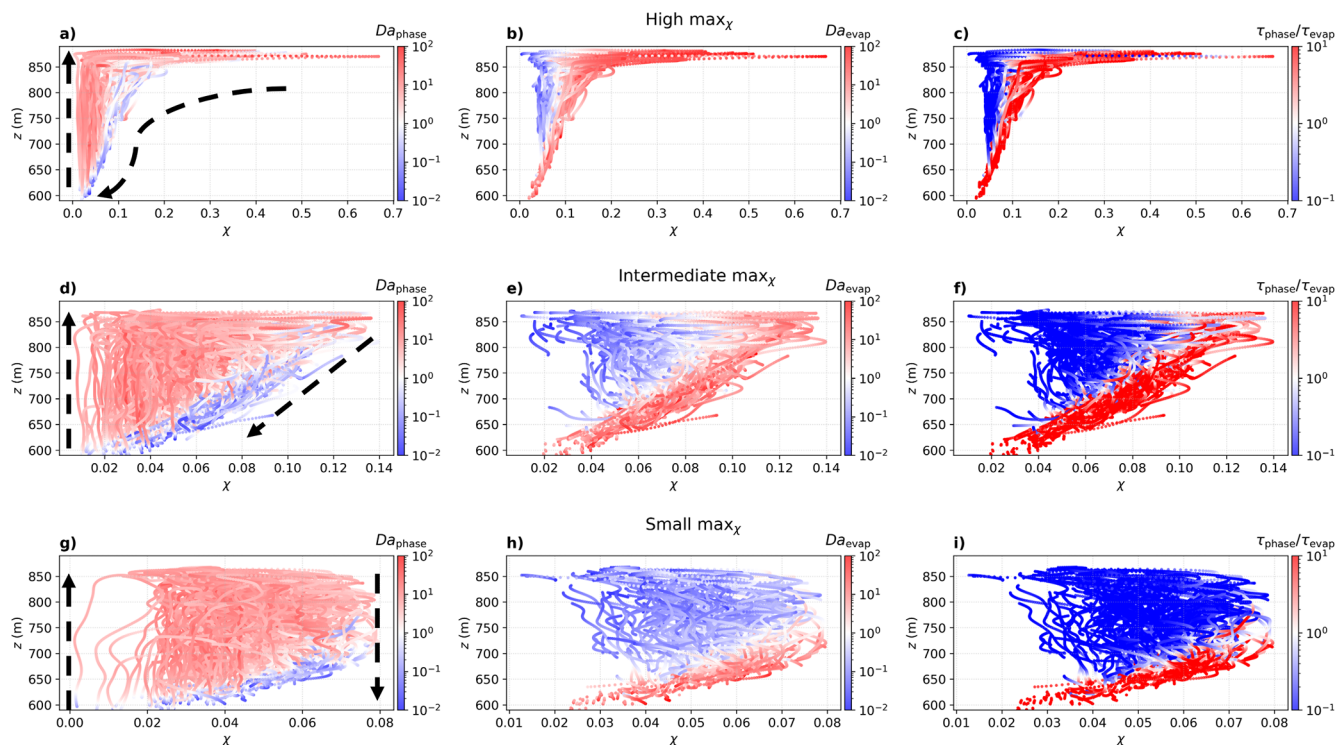


**Figure 11.** Particle trajectories in the  $\chi$ - $z$  phase space, where different colors of dots indicate: the  $Da_{\text{phase}}$  (first column),  $Da_{\text{evap}}$  (second column),  $\tau_{\text{phase}}/\tau_{\text{evap}}$  (third column). The first row shows trajectories with the maximum  $\chi > 0.14$ , the third row shows trajectories where the maximum  $\chi \leq 0.08$ , and the second row shows trajectories with intermediate values, where the maximum  $\chi$  lies between these two conditions. In panels (a), (d), and (g), the dashed black arrows indicate inferred droplet motion directions based on the vertical velocity  $W$ .

approach complete evaporation,  $d_r$  decreases since only a small number of droplets remain. Therefore, this regime is opposite to the *activation regime* with substantial deactivation (Fig. 6l). Note that this regime does not overlap with the *activation regime*, because  $r_m$  and  $d_r$  are generally larger in the *deactivation regime* compared to the *activation regime*, indicating a stronger spatial variability in deactivation. Moreover, since particle trajectories are only tracked for  $q_c > 0$ , an abrupt loss of liquid water near the point of complete evaporation may result in a bias toward retaining large  $r_m$  values as the final recorded state.

#### 4 Complete Expression of Droplet Evolution Pathway

As demonstrated in Sect. 3.2, the growth phase of droplet evolution follows the analytical solution (Eq. 5) derived by Liu et al. (2006), which is grounded in classical diffusional growth theory. Starting from the condensational growth equation

$$\frac{dr}{dt} = \frac{SG}{r}, \quad (12)$$

one may equivalently write  $\frac{1}{2} d(r^2)/dt = SG$ , showing that condensational growth increases  $r^2$  at a rate set by  $S$  and  $G$ .

To relate distribution width to the mean growth, Liu et al. (2006) define a relative deviation  $x = (r - r_m)/r_m$  so that  $r = r_m(1 + x)$  with  $\bar{x} = 0$ . Substituting this into Eq. (12) and linearizing  $1/(1 + x) \approx 1 - x$  yields an evolution equation of the form (their Eq. (4))

$$(1 + x) \frac{1}{2} \frac{d(r_m^2)}{dt} + r_m^2 \frac{dx}{dt} = SG(1 - x). \quad (13)$$

Averaging this over the droplet population yields their Eq. (5):

$$\frac{1}{2} \frac{d(r_m^2)}{dt} = SG. \quad (14)$$

By combining these two equations and using  $d_r^2 = \overline{x^2}$ , this leads to

$$\frac{1}{d_r^2} \frac{d(d_r^2)}{dt} = -2 \frac{1}{r_m^2} \frac{d(r_m^2)}{dt}. \quad (15)$$

Integrating this relationship yields the characteristic inverse-square scaling  $d_r \propto r_m^{-2}$  (Eq. 5), providing a quantitative expression of condensational narrowing during adiabatic ascent. For the full derivation, see Liu et al. (2006) (their Eqs. 2–9).

However, this analytical formulation is insufficient for the decay phase ( $S < 0$ ), where evaporation and mixing induce

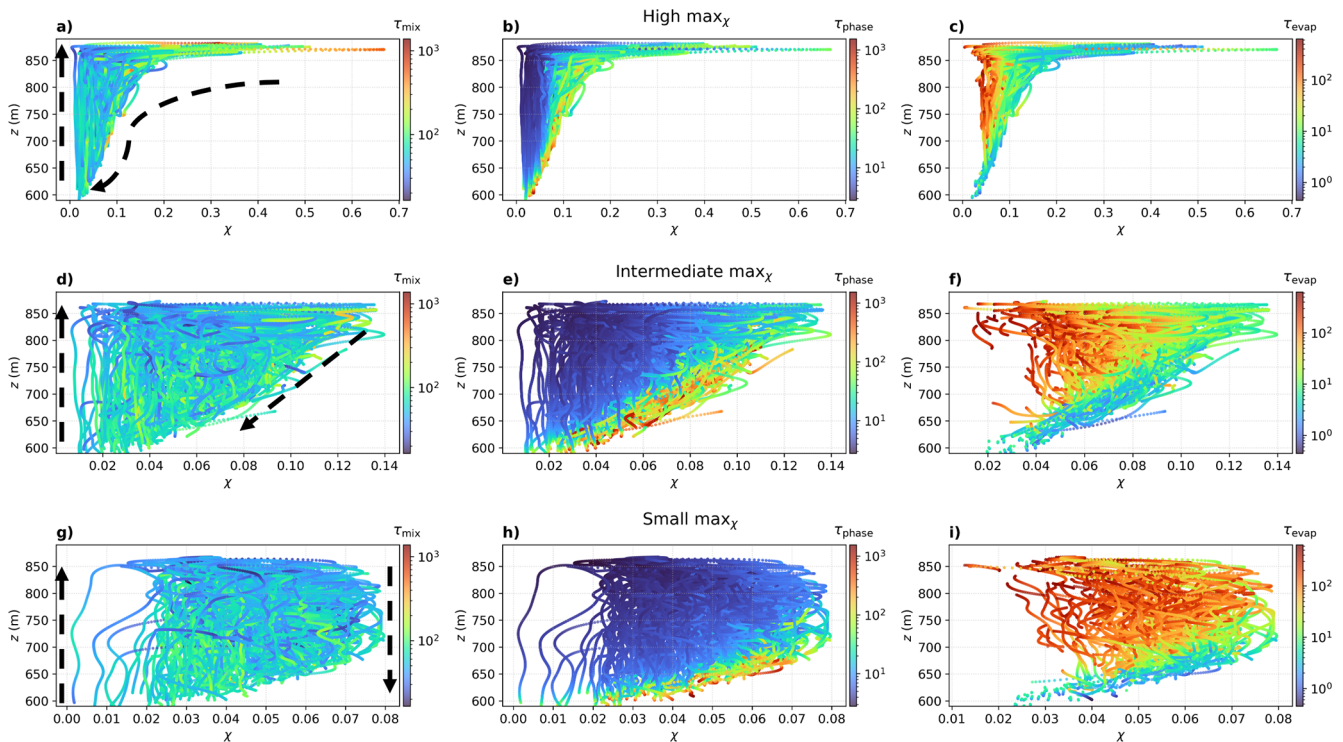


**Figure 12.** Particle trajectories in the  $\chi$ - $z$  phase space, where different colors of dots indicate: the mixing timescale  $\tau_{\text{mix}}$  (first column), the phase-change timescale  $\tau_{\text{phase}}$  (second column), and the evaporation timescale  $\tau_{\text{evap}}$  (third column). The first row shows trajectories with the maximum  $\chi > 0.14$ , the third row shows trajectories where the maximum  $\chi \leq 0.08$ , and the second row shows trajectories with intermediate values, where the maximum  $\chi$  lies between these two conditions. In panels (a), (d), and (g), the dashed black arrows indicate inferred droplet motion directions based on the vertical velocity  $W$ .

nonlinear and path-dependent spectral broadening. While applying Eq. (5) to this regime captures the overall decreasing trend, it fails to reproduce the observed concave curvature, resulting in lower correlation coefficients ( $r^2 = 0.5\text{--}0.8$ ; see light-gray dashed line in Fig. 13). Given that an analytical derivation is complicated by the stochastic nature of entrainment, we instead formulate an empirical model based on geometric constraints. This model is constructed to satisfy two physical boundary conditions observed in our simulations: (1) a maximum dispersion ( $d_{r,\text{max}}$ ) at the limit of small radii, and (2) a vanishing dispersion as the mean radius approaches a system maximum ( $r_{m,\text{max}}$ ), representing the spectral narrowing limit governed by condensational growth.

To satisfy these conditions while capturing the observed curvature, we adopt a quadratic formulation. Combining the analytical growth term with this empirical decay formulation, we propose the following piecewise function for the complete evolution pathway:

$$d_r = \begin{cases} d_{r,0} \frac{r_{m,0}^2}{r_m^2} & \text{if } S \geq 0, \\ d_{r,\text{max}} \left(1 - \frac{r_m^2}{r_{m,\text{max}}^2}\right) & \text{if } S < 0. \end{cases} \quad (16)$$

The results of Eq. (16), fitted to the 50th percentile of the frequency distributions over the final 2 h of simulation, are

shown as solid lines in Fig. 13 for the N50, N100, and N200 cases. The fitted values of  $d_{r,\text{max}}$  are 0.39, 0.40, and 0.41, respectively, while  $r_{m,\text{max}}$  values are 14.9, 11.8, and 9.4  $\mu\text{m}$ , with all fits yielding  $r^2 > 0.98$ . While  $d_{r,\text{max}}$  exhibits only modest variation across aerosol scenarios,  $r_{m,\text{max}}$  decreases noticeably with increasing  $N_a$ , consistent with liquid water being partitioned among a larger number of droplets. The relative insensitivity of  $d_{r,\text{max}}$  to  $N_a$  suggests that a fixed value in the range of 0.3–0.4, commonly observed in stratocumulus clouds (Pawlowska et al., 2006), may serve as a useful approximation.

## 5 Summary and Conclusion

Maritime stratocumulus (Sc) clouds play an important role in Earth's radiative budget by reflecting incoming solar radiation (Wood, 2012). However, our lack of understanding of the variation of key parameters determining the cloud's optical properties, such as the droplet size distribution (DSD), makes clouds a key source of model uncertainty (Boucher et al., 2013). In this study, we investigate the evolution of droplets, focusing on how DSD shape parameters, the mean droplet radius ( $r_m$ ) and droplet radius relative dispersion ( $d_r$ ), evolve by tracking individual cloud droplets. For this purpose, we

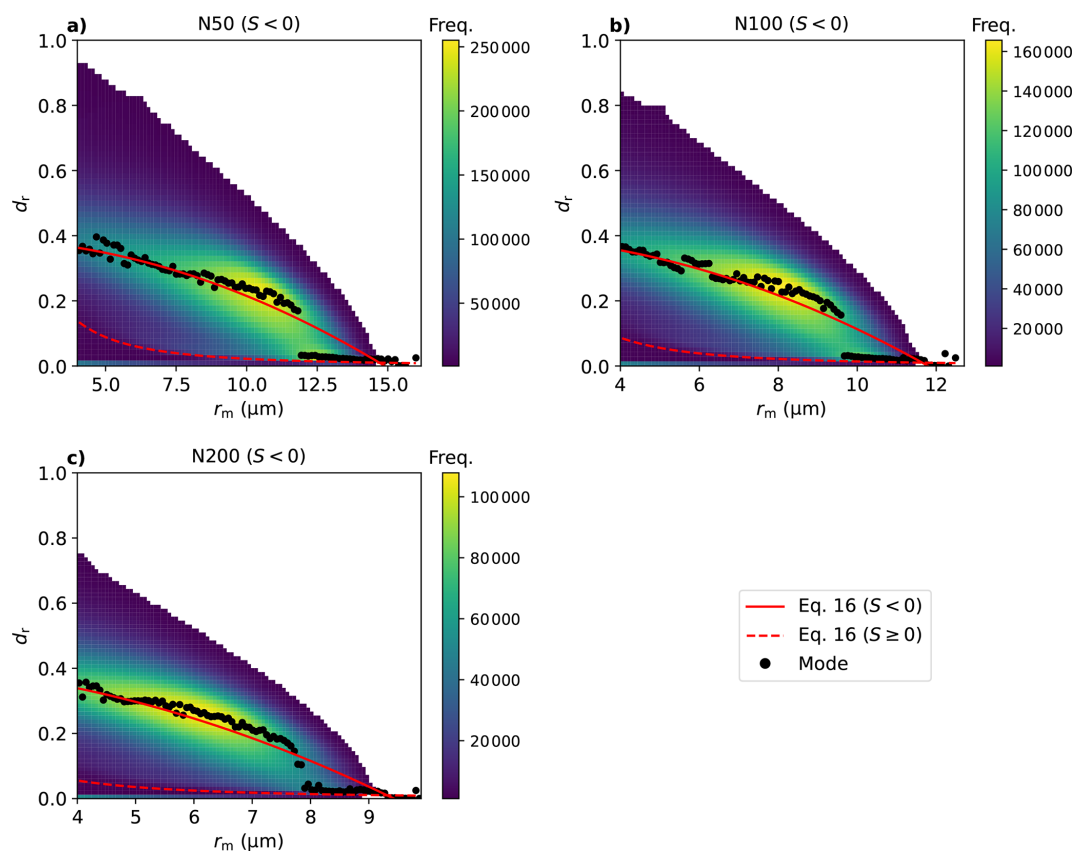


**Figure 13.** Frequency distribution in the  $r_m$ – $d_r$  phase space for  $S < 0$  for the (a) N50, (b) N100, and (c) N200 cases. Black dots represent the most frequent value (mode) in each  $r_m$  bin. The light-gray dashed line shows the fit of the analytical growth-phase equation (Eq. 5) to the  $S < 0$  data. The red lines represent the empirical fits for this evaporation pathway using the final quadratic formulation (the  $S < 0$  part of Eq. 16 as solid and the  $S \geq 0$  part of Eq. 16 as dashed). All fits are based on the median  $d_r$  value in each  $r_m$  bin.

employ the  $L^3$  model that couples a large-eddy simulation (LES) model with a Lagrangian cloud model (LCM), and the linear eddy model (LEM) to accurately represent entrainment and mixing, a key process in determining DSD shape (Lim and Hoffmann, 2023).

We find that the evolution of droplet size distribution (DSD) shape parameters follows characteristic trajectories in the  $r_m$ – $d_r$  phase space, governed by the large-scale circulation of the stratocumulus-topped boundary layer (STBL). Droplets undergo distinct transitions, including activation, condensational growth, entrainment-driven evaporation, and descent within downdrafts, each constituting a stage of an “aging” pathway. Based on supersaturation conditions, we classify the droplet population into four microphysical regimes as follows:

1. Activation ( $S \geq 0$ , small  $r_m$ ): droplets activate, increasing  $r_m$  and broadening  $d_r$ .
2. Adiabatic growth ( $S \geq 0$ , small  $d_r$ ): condensational growth narrows the DSD while increasing  $r_m$ , following the analytical parcel theory ( $d_r \propto r_m^{-2}$ ).

3. Entrainment and descent ( $S < 0$ ): evaporation drives a decrease in  $r_m$  and an increase in  $d_r$ . Critically, droplets in this regime do not follow a single pathway; their trajectories diverge in the  $r_m$ – $d_r$  phase space depending on parcel-specific entrainment history (mixing fraction  $\chi$ ).
4. Deactivation ( $S < 0$ , near cloud base): the final evaporation stage, where large droplets persist longer than small ones, briefly widening  $d_r$  before full deactivation.

Importantly, this study helps resolve a fundamental ambiguity in interpreting mixing mechanisms in stratocumulus clouds. While vertical profiles of droplet number concentration ( $N_c$ ) and mean radius ( $r_m$ ) often suggest a transition from inhomogeneous mixing at cloud top to homogeneous mixing below (Wang et al., 2009; Yum et al., 2015; Yeom et al., 2021), our trajectory-resolved analysis shows that much of this vertical structure arises from sorting of parcels with different entrainment histories within the STBL circulation (Telford and Chai, 1980; Wang et al., 2009). Specifically, the apparent mixing regime is controlled primarily by the Lagrangian entrainment history (summarized by the mixing fraction  $\chi$ ) rather than instantaneous altitude.

Parcels subject to strong entrainment-driven dilution (high  $\chi$ ) exhibit robust inhomogeneous-mixing signatures at cloud top, characterized by a rapid reduction in  $N_c$  with only weak changes in  $r_m$  under strong subsaturation.

In contrast, the pervasive *homogeneous-mixing-like* signature at lower altitudes arises largely from parcels that descend adiabatically within the STBL downdrafts with minimal dilution (low  $\chi$ ). In these parcels,  $r_m$  decreases mainly due to adiabatic warming during descent, while  $N_c$  remains approximately conserved, producing vertical profiles that mimic homogeneous mixing without requiring active entrainment and mixing at that level. These results demonstrate that interpretations based solely on Eulerian snapshots of  $N_c$  and  $r_m$  can conflate local mixing with the imprint of pathway-dependent Lagrangian histories.

Consequently, to provide a more accurate assessment, we suggest using the evaporation-based Damköhler number  $Da_{\text{evap}}$  or the timescale ratio  $\tau_{\text{phase}}/\tau_{\text{evap}}$  as a better parameter for diagnosing mixing scenarios (Pinsky et al., 2016; Fries et al., 2021) than using a  $Da$  based on the single microphysical timescale. This approach is supported by the fact that inhomogeneous mixing is fundamentally controlled by whether a subset of droplets can completely evaporate. In particular,  $\tau_{\text{phase}}/\tau_{\text{evap}}$  depends only on the microphysical state variables  $r_m$ ,  $N_c$ , and  $S$  and does not require explicit knowledge of  $\tau_{\text{mix}}$ , making it particularly attractive. While both  $Da$  values indicate inhomogeneous mixing near the cloud top, each  $Da$  indicates different mixing scenarios during descent without active entrainment events. Therefore, a single  $Da$  may give a false classification of an inhomogeneous to homogeneous mixing scenario, but the combination of both can successfully indicate if the parcel is strongly diluted or not, which is useful to diagnose different entrainment-driven dilution histories.

While our regime classification spans the full vertical structure of the STBL, observational access to this regime space is inherently limited. As a result, the complete trajectory of DSD evolution remains poorly constrained in most field observations. Although some observational studies have reported phase-space patterns consistent with portions of our defined regimes (e.g. Lu et al., 2020), comprehensive vertical coverage is needed to resolve the full aging pathway. Our Lagrangian framework overcomes this methodological limitation by providing a trajectory-resolved depiction of regime transitions across the full STBL depth, offering a coherent framework for interpreting in situ observations within the broader context of cloud evolution.

Building on these regime definitions, we propose an empirical formulation, combined with the analytical expression of Liu et al. (2006), that expresses  $d_r$  as a function of  $r_m$ . This formulation explicitly captures the inverse-square DSD narrowing governed by condensational growth and the nonlinear broadening driven by entrainment and dilution. This unified expression provides a practical framework for incorporating

DSD aging variability into microphysical parameterizations in cloud models.

Our findings underscore the significance of DSD aging in preconditioning the onset of precipitation (e.g. Seifert and Beheng, 2006). Broader DSDs, shaped by diverse droplet growth pathways and entrainment-induced dilution and mixing histories, can enhance the potential for rain formation and reduce a cloud's ability to reflect incoming solar radiation. These results emphasize that droplet-scale evolution under varying thermodynamic and dynamic conditions governs not only the DSD shape but also key radiative and precipitation-relevant properties, highlighting the need for improved representation of DSD variability in large-scale models.

**Code and data availability.** Simulation output used in this study is available from the author upon request. The System for Atmospheric Modeling (SAM) code is publicly available at <http://rossby.msrc.sunysb.edu/SAM.html> (last access: 14 April 2026).

**Author contributions.** JSL conceived the original conceptualization and interpretation of results and model modification. FH provided the base model, contributed to discussions, and provided the funding acquisition for the study and project administration. JSL wrote the original draft, and JSL and FH contributed to the review and editing.

**Competing interests.** The contact author has declared that none of the authors has any competing interests.

**Disclaimer.** Publisher's note: Copernicus Publications remains neutral with regard to jurisdictional claims made in the text, published maps, institutional affiliations, or any other geographical representation in this paper. The authors bear the ultimate responsibility for providing appropriate place names. Views expressed in the text are those of the authors and do not necessarily reflect the views of the publisher.

**Acknowledgements.** The authors gratefully appreciate two anonymous reviewers who helped greatly improve the discussion of this paper. The authors gratefully acknowledge the Gauss Centre for Supercomputing e.V. (<http://www.gauss-centre.eu>, last access: 14 April 2026) for funding this project by providing computing time on the GCS Supercomputer SuperMUC-NG at the Leibniz Supercomputing Centre (<http://www.lrz.de>, last access: 14 April 2026).

**Financial support.** This research has been supported by the Deutsche Forschungsgemeinschaft (grant no. HO 6588/1-1).

The article processing charges for this open-access publication were covered by the Freie Universität Berlin.

**Review statement.** This paper was edited by Minghuai Wang and reviewed by two anonymous referees.

## References

- Ackerman, A. S., van Zanten, M. C., Stevens, B., Savic-Jovicic, V., Bretherton, C. S., Chlond, A., Golaz, J.-C., Jiang, H., Khairoutdinov, M., Krueger, S. K., Lewellen, D. C., Lock, A., Moeng, C.-H., Nakamura, K., Petters, M. D., Snider, J. R., Weinbrecht, S., and Zulauf, M.: Large-eddy simulations of a drizzling, stratocumulus-topped marine boundary layer, *Mon. Weather Rev.*, 137, 1083–1110, 2009.
- Baker, M. and Latham, J.: The evolution of droplet spectra and the rate of production of embryonic raindrops in small cumulus clouds, *J. Atmos. Sci.*, 36, 1612–1615, [https://doi.org/10.1175/1520-0469\(1979\)036%3C1612:TEODSA%3E2.0.CO;2](https://doi.org/10.1175/1520-0469(1979)036%3C1612:TEODSA%3E2.0.CO;2), 1979.
- Baker, M., Corbin, R., and Latham, J.: The influence of entrainment on the evolution of cloud droplet spectra: I. A model of inhomogeneous mixing, *Q. J. Roy. Meteor. Soc.*, 106, 581–598, <https://doi.org/10.1002/qj.49710644914>, 1980.
- Boucher, O., Randall, D., Artaxo, P., Bretherton, C., Feingold, G., Forster, P., Kerminen, V.-M., Kondo, Y., Liao, H., Lohmann, U., Rasch, P., Sathesh, S. K., Sherwood, S., Stevens, B., and Zhang, X. Y.: Clouds and aerosols, in: *Climate change 2013: The physical science basis. Contribution of working group I to the fifth assessment report of the intergovernmental panel on climate change*, Cambridge University Press, 571–657, <https://doi.org/10.1017/CBO9781107415324.016>, 2013.
- Burnet, F. and Brenguier, J.-L.: Observational study of the entrainment-mixing process in warm convective clouds, *J. Atmos. Sci.*, 64, 1995–2011, 2007.
- Chandrakar, K. K., Cantrell, W., and Shaw, R. A.: Influence of turbulent fluctuations on cloud droplet size dispersion and aerosol indirect effects, *J. Atmos. Sci.*, 75, 3191–3209, 2018.
- Chandrakar, K. K., Morrison, H., and Witte, M.: Evolution of droplet size distributions during the transition of an ultraclean stratocumulus cloud system to open cell structure: an LES investigation using Lagrangian microphysics, *Geophys. Res. Lett.*, 49, e2022GL100511, <https://doi.org/10.1029/2022GL100511>, 2022.
- Chen, T., Rossow, W. B., and Zhang, Y.: Radiative effects of cloud-type variations, *J. Climate*, 13, 264–286, 2000.
- Considine, G. and Curry, J. A.: A statistical model of drop-size spectra for stratocumulus clouds, *Q. J. Roy. Meteor. Soc.*, 122, 611–634, 1996.
- Fries, J., Sardina, G., Svensson, G., and Mehlh, B.: Key parameters for droplet evaporation and mixing at the cloud edge, *Q. J. Roy. Meteor. Soc.*, 147, 2160–2172, 2021.
- Gerber, H., Frick, G., Malinowski, S., Brenguier, J., and Burnet, F.: Holes and entrainment in stratocumulus, *J. Atmos. Sci.*, 62, 443–459, 2005.
- Hoffmann, F. and Feingold, G.: Entrainment and mixing in stratocumulus: effects of a new explicit subgrid-scale scheme for large-eddy simulations with particle-based microphysics, *J. Atmos. Sci.*, 76, 1955–1973, <https://doi.org/10.1175/JAS-D-18-0318.1>, 2019.
- Hoffmann, F., Raasch, S., and Noh, Y.: Entrainment of aerosols and their activation in a shallow cumulus cloud studied with a coupled LCM–LES approach, *Atmos. Res.*, 156, 43–57, 2015.
- Hoffmann, F., Yamaguchi, T., and Feingold, G.: Inhomogeneous mixing in Lagrangian cloud models: effects on the production of precipitation embryos, *J. Atmos. Sci.*, 76, 113–133, <https://doi.org/10.1175/JAS-D-18-0087.1>, 2019.
- Jeffery, C. A.: Inhomogeneous cloud evaporation, invariance, and Damköhler number, *J. Geophys. Res.-Atmos.*, 112, <https://doi.org/10.1029/2007JD008789>, 2007.
- Kerstein, A. R.: A linear-eddy model of turbulent scalar transport and mixing, *Combust. Sci. Tech.*, 60, 391–421, <https://doi.org/10.1080/00102208808923995>, 1988.
- Khairoutdinov, M. F. and Randall, D. A.: Cloud resolving modeling of the ARM summer 1997 IOP: model formulation, results, uncertainties, and sensitivities, *J. Atmos. Sci.*, 60, 607–625, [https://doi.org/10.1175/1520-0469\(2003\)060%3C0607:CRMOTA%3E2.0.CO;2](https://doi.org/10.1175/1520-0469(2003)060%3C0607:CRMOTA%3E2.0.CO;2), 2003.
- Korolev, A. and Mazin, I.: Zones of increased and decreased droplet concentration in stratiform clouds, *J. Appl. Meteorol.*, 32, 760–773, 1993.
- Krueger, S. K.: Linear eddy modeling of entrainment and mixing in stratus clouds, *J. Atmos. Sci.*, 50, 3078–3090, [https://doi.org/10.1175/1520-0469\(1993\)050%3C3078:LEMOEA%3E2.0.CO;2](https://doi.org/10.1175/1520-0469(1993)050%3C3078:LEMOEA%3E2.0.CO;2), 1993.
- Krueger, S. K., Su, C.-W., and McMurtry, P. A.: Modeling entrainment and finescale mixing in cumulus clouds, *J. Atmos. Sci.*, 54, 2697–2712, [https://doi.org/10.1175/1520-0469\(1997\)054<2697:MEAFMI>2.0.CO;2](https://doi.org/10.1175/1520-0469(1997)054<2697:MEAFMI>2.0.CO;2), 1997.
- Lehmann, K., Siebert, H., and Shaw, R. A.: Homogeneous and inhomogeneous mixing in cumulus clouds: dependence on local turbulence structure, *J. Atmos. Sci.*, 66, 3641–3659, <https://doi.org/10.1175/2009JAS3012.1>, 2009.
- Lim, J. S.: Entrainment, mixing, and the evolution of the cloud droplet size distribution, PhD thesis, Ludwig-Maximilians-Universität München, Munich, Germany, <https://doi.org/10.5282/edoc.34534>, 2024.
- Lim, J.-S. and Hoffmann, F.: Between broadening and narrowing: how mixing affects the width of the droplet size distribution, *J. Geophys. Res.-Atmos.*, 128, e2022JD037900, <https://doi.org/10.1029/2022JD037900>, 2023.
- Lim, J.-S. and Hoffmann, F.: Life cycle evolution of mixing in shallow cumulus clouds, *J. Geophys. Res.-Atmos.*, 129, e2023JD040393, <https://doi.org/10.1029/2023JD040393>, 2024.
- Liu, Y. and Daum, P. H.: Parameterization of the autoconversion process. Part I: Analytical formulation of the Kessler-type parameterizations, *J. Atmos. Sci.*, 61, 1539–1548, 2004.
- Liu, Y., Daum, P. H., and Yum, S. S.: Analytical expression for the relative dispersion of the cloud droplet size distribution, *Geophys. Res. Lett.*, 33, 2006.
- Liu, Y., Daum, P. H., Guo, H., and Peng, Y.: Dispersion bias, dispersion effect, and the aerosol–cloud conundrum, *Environ. Res. Lett.*, 3, 045021, <https://doi.org/10.1088/1748-9326/3/4/045021>, 2008.
- Lu, C., Liu, Y., Zhu, B., Yum, S. S., Krueger, S. K., Qiu, Y., Niu, S., and Luo, S.: On which microphysical time scales to use in studies of entrainment-mixing mechanisms in clouds, *J. Geophys. Res.-Atmos.*, 123, 3740–3756, 2018a.
- Lu, C., Sun, C., Liu, Y., Zhang, G. J., Lin, Y., Gao, W., Niu, S., Yin, Y., Qiu, Y., and Jin, L.: Observational relationship between entrainment rate and environmental relative humidity and impli-

- cations for convection parameterization, *Geophys. Res. Lett.*, 45, 13–495, 2018b.
- Lu, C., Liu, Y., Yum, S. S., Chen, J., Zhu, L., Gao, S., Yin, Y., Jia, X., and Wang, Y.: Reconciling contrasting relationships between relative dispersion and volume-mean radius of cloud droplet size distributions, *J. Geophys. Res.-Atmos.*, 125, e2019JD031868, <https://doi.org/10.1029/2019JD031868>, 2020.
- Luo, S., Lu, C., Liu, Y., Li, Y., Gao, W., Qiu, Y., Xu, X., Li, J., Zhu, L., Wang, Y., Wu, J., and Yang, X.: Relationships between cloud droplet spectral relative dispersion and entrainment rate and their impacting factors, *Adv. Atmos. Sci.*, 39, 2087–2106, <https://doi.org/10.1007/s00376-022-1419-5>, 2022.
- Mellado, J. P.: Cloud-top entrainment in stratocumulus clouds, *Annu. Rev. Fluid Mech.*, 49, 145–169, 2017.
- Pawłowska, H., Grabowski, W. W., and Brenguier, J.-L.: Observations of the width of cloud droplet spectra in stratocumulus, *Geophys. Res. Lett.*, 33, <https://doi.org/10.1029/2006GL026841>, 2006.
- Pinsky, M., Khain, A., Korolev, A., and Magaritz-Ronen, L.: Theoretical investigation of mixing in warm clouds – Part 2: Homogeneous mixing, *Atmos. Chem. Phys.*, 16, 9255–9272, <https://doi.org/10.5194/acp-16-9255-2016>, 2016.
- Seifert, A. and Beheng, K. D.: A two-moment cloud microphysics parameterization for mixed-phase clouds. Part 1: Model description, *Meteorol. Atmos. Phys.*, 92, 45–66, 2006.
- Shima, S., Kusano, K., Kawano, A., Sugiyama, T., and Kawahara, S.: The super-droplet method for the numerical simulation of clouds and precipitation: a particle-based and probabilistic microphysics model coupled with a non-hydrostatic model, *Q. J. Roy. Meteor. Soc.*, 135, 1307–1320, <https://doi.org/10.1002/qj.441>, 2009.
- Siebesma, A. P., Jakob, C., Lenderink, G., Neggers, R. A. J., Teixeira, J., Van Meijgaard, E., Calvo, J., Chlond, A., Grenier, H., Jones, C., Köhler, M., Kitagawa, H., Marquet, P., Lock, A. P., Müller, F., Olmeda, D., and Severijns, C.: Cloud representation in general-circulation models over the northern Pacific Ocean: a EUROCS intercomparison study, *Q. J. Roy. Meteor. Soc.*, 130, 3245–3267, 2004.
- Squires, P.: The growth of cloud drops by condensation. I. General characteristics, *Aust. J. Chem.*, 5, 59–86, <https://doi.org/10.1071/CH9520059>, 1952.
- Stevens, B.: Entrainment in stratocumulus-topped mixed layers, *Q. J. Roy. Meteor. Soc.*, 128, 2663–2690, 2002.
- Stevens, B., Lenschow, D. H., Vali, G., Gerber, H., Bandy, A., Blomquist, B., Brenguier, J.-L., Bretherton, C. S., Burnet, F., Campos, T., Chai, S., Faloon, I., Friesen, D., Haimov, S., Laursen, K., Lilly, D. K., Loehrer, S. M., Malinowski, S. P., Morley, B., Petters, M. D., Rogers, D. C., Russell, L., Savic-Jovicic, V., Snider, J. R., Straub, D., Szumowski, M. J., Takagi, H., Thornton, D. C., Tschudi, M., Twohy, C., Wetzell, M., and van Zanten, M. C.: Dynamics and chemistry of marine stratocumulus – DYCOMS-II, *B. Am. Meteorol. Soc.*, 84, 579–594, 2003.
- Telford, J. W. and Chai, S. K.: A new aspect of condensation theory, *Pure Appl. Geophys.*, 118, 720–742, 1980.
- Tölle, M. H. and Krueger, S. K.: Effects of entrainment and mixing on droplet size distributions in warm cumulus clouds, *J. Adv. Model. Earth Sy.*, 6, 281–299, <https://doi.org/10.1002/2012MS000209>, 2014.
- Virtanen, P., Gommers, R., Oliphant, T. E., Haberland, M., Reddy, T., Cournapeau, D., Burovski, E., Peterson, P., Weckesser, W., Bright, J., van der Walt, S. J., Brett, M., Wilson, J., Millman, K. J., Mayorov, N., Nelson, A. R. J., Jones, E., Kern, R., Larson, E., Carey, C. J., Polat, İ., Feng, Y., Moore, E. W., VanderPlas, J., Laxalde, D., Perktold, J., Cimrman, R., Henriksen, I., Quintero, E. A., Harris, C. R., Archibald, A. M., Ribeiro, A. H., Pedregosa, F., van Mulbregt, P., and SciPy 1.0 Contributors: SciPy 1.0: fundamental algorithms for scientific computing in Python, *Nat. Methods*, 17, 261–272, <https://doi.org/10.1038/s41592-019-0686-2>, 2020.
- Wang, J., Daum, P. H., Yum, S. S., Liu, Y., Senum, G. I., Lu, M.-L., Seinfeld, J. H., and Jonsson, H.: Observations of marine stratocumulus microphysics and implications for processes controlling droplet spectra: results from the Marine Stratus/Stratocumulus Experiment, *J. Geophys. Res.-Atmos.*, 114, <https://doi.org/10.1029/2008JD011035>, 2009.
- Wang, Y., Zhao, C., McFarquhar, G. M., Wu, W., Reeves, M., and Li, J.: Dispersion of droplet size distributions in supercooled non-precipitating stratocumulus from aircraft observations obtained during the southern ocean cloud radiation aerosol transport experimental study, *J. Geophys. Res.-Atmos.*, 126, e2020JD033720, <https://doi.org/10.1029/2020JD033720>, 2021.
- Wood, R.: Stratocumulus clouds, *Mon. Weather Rev.*, 140, 2373–2423, 2012.
- Yang, F., Shaw, R., and Xue, H.: Conditions for superadiabatic droplet growth after entrainment mixing, *Atmos. Chem. Phys.*, 16, 9421–9433, <https://doi.org/10.5194/acp-16-9421-2016>, 2016.
- Yau, M. K. and Rogers, R. R.: *A Short Course in Cloud Physics*, Elsevier, ISBN 978-0-7506-3215-7, 1996.
- Yeom, J. M., Yum, S. S., Shaw, R. A., La, I., Wang, J., Lu, C., Liu, Y., Mei, F., Schmid, B., and Matthews, A.: Vertical variations of cloud microphysical relationships in marine stratocumulus clouds observed during the ACE-ENA campaign, *J. Geophys. Res.-Atmos.*, 126, e2021JD034700, <https://doi.org/10.1029/2021JD034700>, 2021.
- Yum, S. S., Wang, J., Liu, Y., Senum, G., Springston, S., McGraw, R., and Yeom, J. M.: Cloud microphysical relationships and their implication on entrainment and mixing mechanism for the stratocumulus clouds measured during the VOCALS project, *J. Geophys. Res.-Atmos.*, 120, 5047–5069, 2015.